Chemistry and kinematics of stars in Local Group galaxies

Battaglia, Giuseppina

Chapter 5

The mass content of the Sculptor Dwarf Spheroidal Galaxy

G. Battaglia, A. Helmi, E. Tolstoy, M. J. Irwin

paper in preparation

ABSTRACT– We derive the line-of-sight (l.o.s.) velocity dispersion profile of the Sculptor dwarf spheroidal galaxy using the VLT/FLAMES low resolution spectra of Red Giant Branch stars presented in Chapters 2 and 4. Our data extend out to and beyond Sculptor nominal tidal radius. The l.o.s. velocity dispersion for all Sculptor stars is approximately constant around 9 km s^{-1} out to the last measured point at $r = 1.3$ deg (1.8 kpc, i.e. 13.3 core radii).

We also derive separately the dispersion profiles of the metal rich (MR) and metal poor (MP) populations known to be present in Sculptor. The MR l.o.s. velocity dispersion is $\sim$ 9 km s^{-1} in the central regions and then declines to $\sim$ 2 km s^{-1} at 0.5 deg. The profile for the MP stars is relatively flat and reflects the behaviour of the global dispersion profile, in agreement with the fact that this is the dominant population in Sculptor.

We compare these observed l.o.s. profiles to predictions from dark matter models. The model that best fits the data is an isothermal profile with core radius $r_c = 0.5$ kpc and mass enclosed within the last measured point $3.4 \pm 0.7 \times 10^8$ $M_\odot$ assuming an increasingly radially anisotropic velocity ellipsoid. In this model the mass-to-light ratio is 158$\pm$33 $(M/L)_\odot$ inside 1.8 kpc. Cosmologically motivated models such as an NFW profile with $c = 20$ and virial mass $M_v = 2.2^{+1.0}_{-0.7} \times 10^9$ $M_\odot$ also provide a fit which is statistically consistent with the observations, but they tend to yield poorer fits for the MR stars. The combined modeling of the two populations has the important advantage of breaking some of the degeneracies present in modeling Sculptor as a single component galaxy.

5.1 Introduction

DWARF spheroidal galaxies (dSphs) are the smallest objects which require the presence of dark matter (DM) to explain their kinematics in the context of Newtonian gravity and they are also the most DM dominated kind of systems.

dSphs have similar luminosities ($10^5, 10^6\,L_\odot$) and central velocity dispersions (6-10 km s^{-1}) to globular clusters (GCs), but they are much more extended, with half-light radii of hundreds of parsecs, about one order of magnitude larger than for GCs. This has an important implication: assuming that both these systems are in equilibrium, the virial theorem implies no DM for GCs (Illingworth 1976; Pryor et al. 1988), while large amounts are required to sustain the dispersion observed in dSphs.

This was first hinted at in the work of Aaronson (1983), who derived an M/L ratio of 30 $(M/L)_\odot$ for the Draco dSph by measuring its central velocity dispersion with three carbon stars. Despite the small number statistics and the problems connected with the use of carbon stars to measure velocities, this suggested a large amount of unseen matter in this galaxy. Since then numerous works have been carried out to measure the DM content of dSphs. For a long time these measurements were based just on the central value of the dispersion and on the hypothesis that mass follows light (e.g., Mateo et al. 1991; Suntzeff et al. 1993; Hargreaves et al. 1994, 1996). The advent of large telescopes with multi-fibres spectrographs has made the derivation of velocity dispersion *profiles* possible for most of the dSphs around the Milky Way (MW), allowing more sofisticated and accurate mass modeling (e.g., Kleyna et al. 2003; Wilkinson et al. 2006; Walker et al. 2006). These more recent works were able to rule out the hypothesis that mass follows light, and this implies that dSphs must be embedded in extended DM haloes. Furthermore, mass-to-light ratios of several 100s $(M/L)_\odot$ have been derived, which makes dSphs the most DM dominated objects known to date.

However, the presence of DM in dSphs has been regularly questioned. The debate as to whether dSphs have DM or not has been driven by the fact that dSphs are small galaxies which (in general) orbit much larger systems. For instance, in the Local Group the great majority of dSphs are found within 300 kpc of the MW or M31 and are thus susceptible to experience strong interactions with the potential of the host. This raises the question as to whether these systems are in equilibrium or if the large observed velocity dispersion might merely be the result of tidal disruption. For example Kroupa (1997) and Klessen & Kroupa (1998) found in numerical simulations that tidally disrupted systems with no DM could reproduce the photometric and kinematic properties of dSphs. These issues have triggered many studies looking for possible signs of tidal disturbance in dSphs such as tidal tails, broadening of the horizontal branch (HB) width and velocity gradients, as predicted by the models. Until now possible signs of disturbance have been found only in the Carina (see Muñoz et al. 2006, and references there in) and Ursa Minor dSphs (Bellazzini et al. 2002; Palma et al. 2003), although the latter case is somewhat controversial. It is interesting that no tidal signatures have been found in Draco (e.g. Ségall et al. 2007), which has a mass-to-light ratio of $\sim$300 $(M/L)_\odot$ (Kleyna et al. 2001), one of the largest ever measured.

Given that so few signs of tidal disruption have been found, we can assume that most dSphs are in equilibrium. We can thus use these objects as a good test ground for DM theories as the study of the DM mass content and distribution on small scales

can put important constraints on the nature of DM (e.g., hot, warm, cold).

A prediction of DM theories of structure formation is the mass spectrum of virialized structures. In this context "hot" DM can be excluded because it does not cluster on such small scales as dSphs (e.g. Lin & Faber 1983; Gerhard & Spergel 1992). The currently most succesful theory of galaxy formation in a cosmological context is based on Cold DM (CDM). This theory however faces problems on the small galactic scales. One of the most well-known issues is the "missing satellites problem": CDM theories predict the presence of 100-1000s bound substructures (subhaloes) surrounding a galaxy like the MW (Moore et al. 1999; Klypin et al. 1999), whilst until two years ago there were only 11 known MW satellites. This mismatch of 1-2 orders of magnitude between the number of predicted and observed satellites has been somewhat mitigated by the discovery of about 10 new low luminosity MW satellites in the past two years by SDSS (Willman et al. 2005a,b; Zucker et al. 2006a,b; Belokurov et al. 2006, 2007; Walsh et al. 2007). Whilst this suggests that the observed satellites might be the "tip of the iceberg", at the moment observations and CDM simulations are still far from being fully reconciled.

A solution to the "missing satellites problem" was suggested by Stoehr et al. (2002) and Hayashi et al. (2003), who proposed that the observed satellites might inhabit the $\sim$10 most massive DM subhaloes, implying that the mass of dSphs had been strongly underestimated. They predicted these subhaloes to have peak circular velocities, $v_{\rm max}$, exceeding 35 km s^{-1} (Hayashi et al. 2003) and a *present* mass of $\sim 10^9\ M_\odot$ (Stoehr et al. 2002), whilst haloes with lower peak circular velocities would "lack readily detectable luminous counterparts" (Hayashi et al. 2003). Other solutions consider the effect that the photoionizing background due to the reionization of the Universe has on the formation of small galactic systems, proposing that after reionization gas accretion and/or star formation is halted in systems with $v_{\rm max} < 30$ km s^{-1} ; many dSphs should thus have formed their stars before reionization in larger subhaloes (Bullock et al. 2000; Benson et al. 2002; Kravtsov et al. 2004). Accurate measurements of the mass in dSphs and fainter recent discoveries can help in confirming or disproving this hypothesis.

Another prediction that different theories provide is the density distribution of DM. In the case of WDM, cored density profiles are expected (Dalcanton & Hogan 2001; Kaplinghat 2005; Cembranos et al. 2005; Strigari et al. 2007c), whilst CDM predicts them to be cusped (Dubinski & Carlberg 1991; Diemand et al. 2005). Specifically, in the case of CDM theories of structure formation virialized objects should follow an Navarro, Frenk & White (NFW) density profile (Navarro, Frenk, & White 1996, 1997) on every scale, from galaxy clusters to the smallest dwarf galaxies. Here again CDM encounters problems on the small scales: whilst the density profiles of galaxy clusters and large galaxies are compatible with cuspy NFW profiles, this is not the case for some low surface brightness galaxies (e.g. Flores & Primack 1994; Moore 1994; McGaugh & de Blok 1998; de Blok et al. 2001). However it has been argued that these galaxies rotation curves might have suffered from several effects, including instrumental ones such as for instance due to beam-smearing or physical effects such as presence of bars, triaxiality, which could prevent definitive conclusions on the subject (e.g. Hayashi & Navarro 2006). For dSphs, i.e. on the smallest scales, several studies of the DM density distribution (see Wilkinson et al. 2006; Walker et al. 2006; Koch et al. 2007, and references there in) have shown that cores are compatible with the observations,

although cusps cannot be excluded. Thus the debate is still open.

In this chapter we derive the mass content and distribution of the Sculptor (Scl) dSph using our spatially extended and accurate spectroscopic dataset obtained at VLT/FLAMES (Chapter 4). The previous mass determination for Scl dates back to the work of Queloz et al. (1995). Using velocities for 23 Scl RGB stars in the central regions, they derived a moderate mass-to-light ratio of 13±6 $(M/L)_{\odot}$, resulting in a mass of $\sim 3 \times 10^7\ M_{\odot}$. Recently Westfall et al. (2006) derived a velocity dispersion profile for Scl out to 50 arcmin (using 147 stars), well within its nominal tidal radius (see previous chapter), but they did not carry out a mass modeling.

5.2 The observational sample

The observational sample has already been described in Chapter 4. Here we remind the reader that our spectroscopic targets were chosen from a box on the Scl CMD (Fig. 4.2, Chapter 4) such that the stars have magnitudes and colours consistent with being Scl Red Giant Branch stars.

After applying quality selection criteria we obtained velocities and metallicities for 470 Sculptor probable members, where the probable members are stars whose velocity falls within 3σ from the systemic velocity. The spatial location of these stars is shown in Fig. 4.6 (Chapter 4).

5.3 Observed velocity dispersion profile

Velocity dispersion profiles are commonly used to study the mass content of a galaxy. In resolved stellar population studies, velocity dispersion profiles are derived from the measurement of velocities of individual stars, which are in general selected from a specific region on a CMD. As can be seen in Fig. 4.2 (Chapter 4), these selection regions are bound to contain a certain amount of interlopers, i.e. stars which do not belong to the object under study. In our case most of the contaminants will be foreground stars from the MW.

As the kinematics of these interlopers are unrelated to the object under study and do not trace the object mass distribution, it is important to clean up the sample from these objects.

We can divide the methods for interlopers' removal in two basic kinds: a direct and a statistical approach. In the direct approach it is possible to physically identify which stars are contaminants and remove them. In the statistical approach instead assumptions are made on the expected amount of contaminations, and the "suspected contaminants" are either removed or their presence is taken into account in a statistical sense.

At the magnitudes and colours considered here, the contamination from the MW is most likely given by dwarf stars in the thin and thick disks. Since dwarfs have a much higher surface gravity than RGB stars it is possible to use gravity indicators as dwarf/giant discriminators (direct approach). For example, Washington M, T2 + DDO51 photometry, which uses the gravity sensitivity of the Mg triplet and MgH line

at 5150 Å, has proved to be a very successful dwarf/giants discriminator (e.g., Majewski et al. 2000; Morrison et al. 2001).

However our V, I photometry is not suitable as discriminator, and the spectral range covered by our data is from 8200 Å to 9000 Å , thus not including the Mg lines at $\sim$ 5000 Å. Hence here we do not use a direct approach in order to separate the contaminants from Scl*.

Below we describe the two different statistical approaches we use to deal with the presence of interlopers and derive the observed dispersion profile: first we describe the traditional 3-σ clipping and then we introduce a more sofisticated maximum likelihood approach. Finally we present first the global Scl l.o.s. velocity dispersion profile, derived without separating the stars according to their metallicity, and then for the MR and the MP components separately.

Beside the issue of contamination, the velocity dispersion profile will need to be corrected for the rotation signal found in Scl, described in Chapter 4. This is necessary because a rotational signature may artificially inflate the measured dispersion.

Our velocity dispersion profile will be obtained by binning the velocities of stars at similar radii. Besides the issue of the optimal binning, it is also worthwhile exploring the choice of how to bin the data: in elliptical or in circular annuli. In fact, one uses stars with a non-spherical spatial distribution as kinematic tracers of an underlying mass distribution which might be spherical (as well as oblate, prolate or even triaxial).

All of these effects are taken into account in both our statistical approaches when deriving the global velocity dispersion profile and the two components profiles, but we discuss these in more detail in the case of the 3-σ clipping approach for the global profile.

5.3.1 3-σ clipping

The statistical approach commonly used to separate dSph members from MW stars is to iteratively apply a k-σ cut on the observed velocity distribution (e.g., see Fig. 4.5 in Chapter 4). The k-σ cut in common use is the 3σ which is justified by the fact that the velocity distribution of stars in dSphs (as well as the velocity distribution of galaxies in clusters) is close to Gaussian (see Wojtak et al. 2007, for references, more discussion and tests). With this method those objects whose velocity exceeds the 3σ limit are removed from the sample.

Here we apply this method to the Scl dataset, considering as probable members those stars with heliocentric velocity in the range $v_{\rm sys} \pm 3\sigma_{\rm los}$, as described in Chapter 4.

We derive the velocity dispersion profile for these stars both imposing bins of constant width and also fixing the number of stars per bin to a constant value (Fig. 5.1), i.e. N=40 with the exception of the last bin which contains 30 stars. A smaller number of stars per bin is not desirable as it causes the velocity dispersion profile to be too noisy. The binning is done in elliptical annuli of constant ellipticity and position angle (e =0.32, P.A.= 99°), to follow the projected shape of the stars spatial distribution. We also allow the average velocity per bin to vary, and derive the dispersion with respect to the average velocity in each bin (we will come back to this point later). We consider

* We will explore the use of the MgI line at 8807 Å as a possible direct dwarf/giant discriminator in a future work.

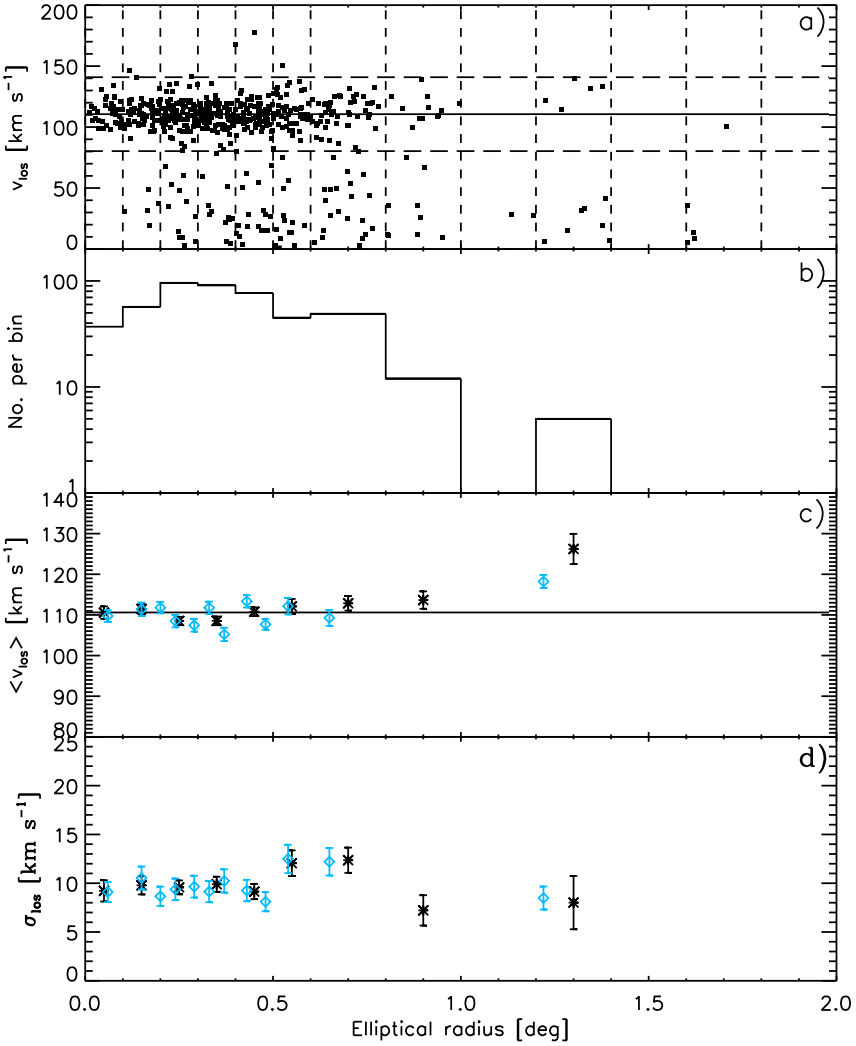

Figure 5.1: Kinematic properties of probable Scl members for the binning we use in our analysis. From top to bottom: l.o.s. heliocentric velocity versus elliptical radius (a); number of stars (b); average l.o.s. velocity (c, asterisks); l.o.s. velocity dispersion for 3σ members (d, asterisks). In panel a) the solid line indicates the systemic velocity, the horizontal long-dashed lines show the region used for the 3σ membership selection and the vertical dashed lines show the binning. For comparison we show the average l.o.s. velocity and the l.o.s. velocity dispersion profile derived fixing the number of stars per bin to $N = 40$, with the exception of the last bin which contains 30 stars (diamonds in panels c and d).

as the error in the variance $\delta var = \sqrt{2\sigma^4_{\rm tot}/N}$, where N is the number of stars per bin and $\sigma^2_{\rm tot} = \sigma^2 + < \sigma^2_{\rm meas} >$ (see Hargreaves et al. 1994). Here σ is the dispersion in the bin and $< \sigma^2_{\rm meas} >$ is the variance due to the measured errors in the velocities. Here the contribution of the latter is always very small compared to the measured dispersion. Finally, the error in the dispersion is $\frac{\delta var}{2\sigma}$.

We find that the constant width binning and N=40 binning (Fig. 5.1) give very similar results and the derived velocity dispersion profile is almost constant around a value of ~ 9 km s^{-1}, with an hint of decline in the last measured point. *In the following we adopt the binning with fixed bin size*, which in general has a larger number of points per bin and it is smoother.

Figure 5.1a,c also shows that at $r \gtrsim 0.7$ deg the value of the average velocity per bin departs from the systemic velocity. This is likely due to a combination of the rotation signal (see Chapter 4) and the fact that in this distance range our coverage is biased towards the west part of Scl, where there is an excess of stars with "receding velocities". The larger dispersion at $r \sim 0.6$ deg might be in part due to this effect.

We point out that the bin centered at 1.3 deg is peculiar; of the 5 stars present in this bin, 3 have large receding velocities with respect to the systemic ($v_h > 130$ km s^{-1}). These 3 stars are located close to the projected major axis, in the east side of the galaxy (ξ [deg] $\sim +1.3$, $-0.2 < \eta$ [deg] $< +0.2$), which from our rotation analysis (see Chapter 4) should be the approaching part. It seems likely that these 3 stars are contaminants.

Elliptical versus circular binning: Analysis of the velocity moments fields in elliptical galaxies (see for example Emsellem et al. 2004; Douglas et al. 2007) shows that the contours of constant l.o.s. velocity dispersion have approximately the same shape and orientation as the light distribution. Therefore mapping the kinematic behaviour along circular annuli would mix together stars with different kinematics. However, dwarf spheroidal galaxies appear to be much more DM dominated than large ellipticals, thus the underlying DM potential might influence much more strongly the shape of the equi-$\sigma_{\rm los}$ contours. The relation between the potential and the shape of the equi-$\sigma_{\rm los}$ contours is not trivial as it also depends on the viewing angle and on the distribution and kinematics of the stars (e.g. Lanzoni & Ciotti 2003, see also Eq. 5.12).

Since we do not have any constraints on the inclination, we opt for an empirical approach to explore the effect of binning the data following the shape of the light distribution. The velocity dispersion profile derived with the circular binning is shown in Fig. 5.2. The differences with respect to the dispersion profile derived with the elliptical binning are negligible, as the two profiles are everywhere consistent with each other at the 1σ level. This is probably due to the fact that our coverage is mostly sampling roughly along the major axis, where circular and elliptical radii coincide. The lower value of the velocity dispersion in the last bin is due to the 3 peculiar stars mentioned above, found at ξ [deg] $\sim +1.3$, $-0.2 < \eta$ [deg] $< +0.2$.

In the remainder of the paper we adopt elliptical binning.

Removing the rotation signal: To explore the effect of rotation we re-derived the velocity dispersion profile by removing the observed rotation signal. Accurately removing the rotation signal in principle requires knowledge of the global rotation pattern, however, as we saw in Chapter 4, it is difficult to establish exactly how the

system is rotating (e.g., $v_{\rm rot} = f(x, y)$ or $v_{\rm rot} = f(x)$ etc) with the present spatial sampling. We adopt a simple empirical approach and assume that $v_{\rm rot} = kx$, where $k = -7.6$ km s^{-1} deg^{-1} is the measured velocity gradient along the major axis and x is simply the projected abscissa on the sky. We subtract $v_{\rm rot}$ from the observed GSR velocities, and propagate the error in the measured rotation signal onto the individual velocity errors. After this subtraction, the velocity field and the average velocity along the major axis are consistent with no rotation.

The velocity dispersion profile derived from these rotation-corrected GSR velocities is shown in Fig. 5.3. Now the average velocity per bin at $r \gtrsim 0.7$ deg is consistent with the systemic velocity (except in the last bin, the causes have already been discussed above). This shows that, as anticipated, the variation of the systemic velocity with radius was a combination of the rotation signal and the asymmetric coverage.

In the remainder of the chapter we use the rotation-subtracted GSR velocities to derive velocity dispersion profiles.

5.3.2 Statistical approach

To apply a sharp k-σ cut to the whole sample in order to remove interlopers might cause some problems.

The choice of the appropriate cut depends not only on the assumption that the dSph velocity distribution is Gaussian but also on the amount of MW contamination one expects given the bulk velocity of the system. For instance, we found that a 2.5-σ cut is preferable to a 3-σ cut to limit the contamination in the case of the Fornax dSph (Chapter 3), where the velocity distribution is heavily affected by MW foreground due to its low heliocentric velocity ($v_{\rm sys} = 54.1$ km s^{-1}).

Finally, since there is no sharp distinction between the velocity distribution of MW and dSphs stars, the k-σ method does not take into account that a percentage of MW stars will fall within the k-σ range. This percentage will increase the farther out we go from the centre of the galaxy as a consequence of the decreasing ratio between dSph and MW densities.

In what follows we describe the more complete statistical approach we use to derive the l.o.s. velocity dispersion of the Scl dSph. Our aim is take into account the MW foreground contamination in the most reliable way possible. This means deriving the level of contaminants in the region of the CMD that we used to select our targets, how this is distributed in l.o.s. velocity and how its relative contribution to the Scl signal changes with radius.

Relative number of stars We derive the expected numbers of RGB stars in Scl and the MW contaminants in the selection region of the CMD from the observed RGB surface density profile and relative foreground density derived from the photometric analysis in Sect. 4.3.2. This allows us to determine the fraction of MW and Scl RGB stars per distance bin, $N_{\rm MW}(r_1 < r < r_2)/N_{\rm TOT}(r_1 < r < r_2)$, $N_{\rm dSph}(r_1 < r < r_2)/N_{\rm TOT}(r_1 < r < r_2)$, where $N_{\rm TOT}(r_1 < r < r_2) = N_{\rm MW}(r_1 < r < r_2) + N_{\rm dSph}(r_1 <$

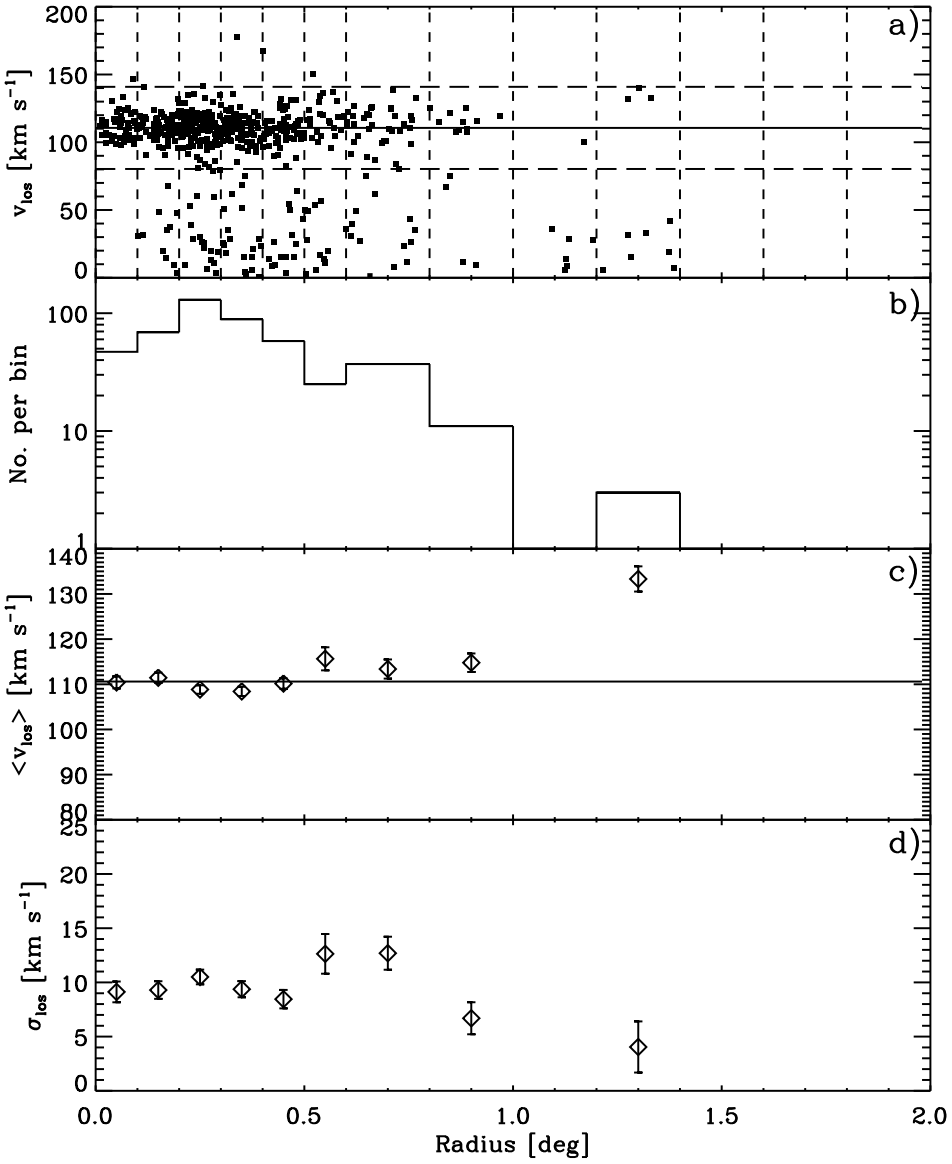

Figure 5.2: As Fig. 5.1 but the distance from the centre is the circular radius.

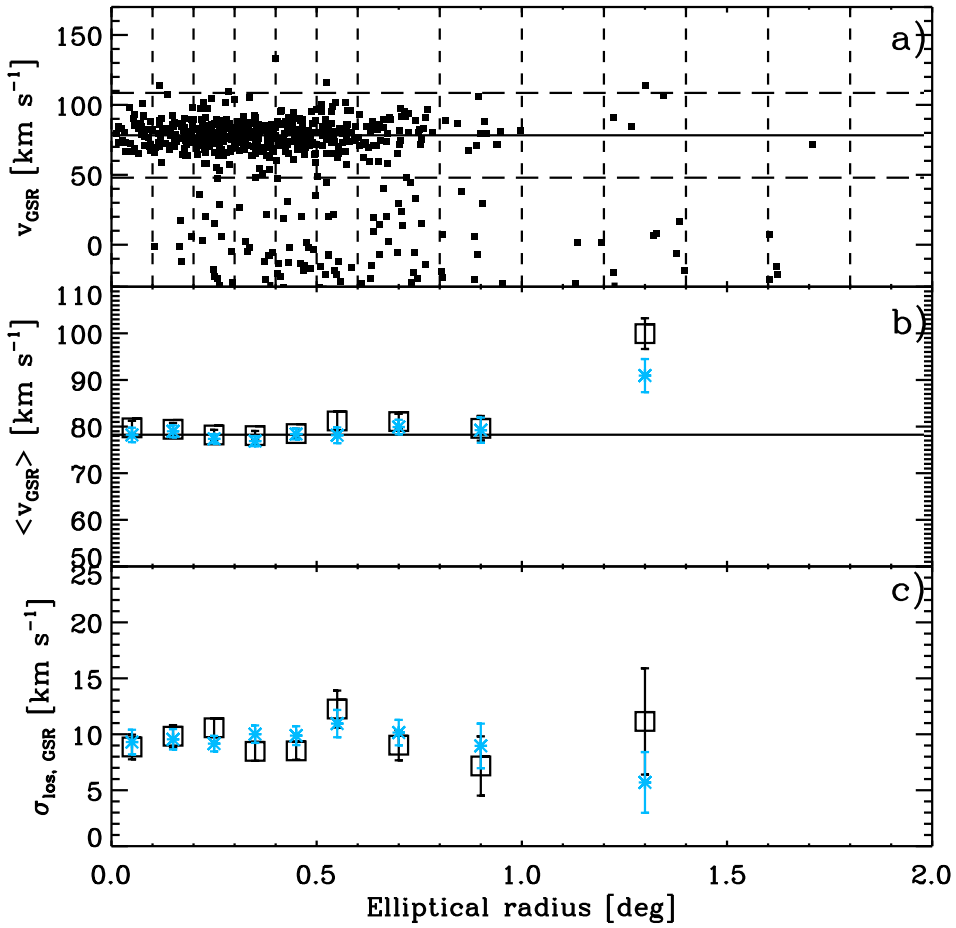

Figure 5.3: Variation of rotation-subtracted GSR velocity with elliptical radius (a), average rotation-subtracted GSR velocity (b), velocity dispersion profile using rotation-subtracted GSR velocities (c). In panels (b) and (c) the asterisks show the properties derived from the 3σ members and the squares show the properties derived using the statistical method presented in Sect. 5.3.2. The solid line in panel (a) and (b) indicates the systemic velocity in the GSR system ($v_{\rm sys,GSR} = 78.3$ km s^{-1}). We propagated the error in the subtracted rotation signal onto the measured velocity errors of the individual stars.

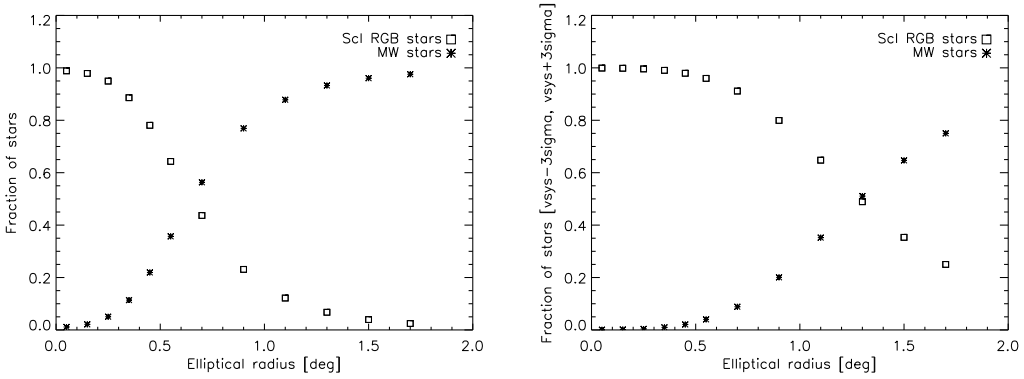

Figure 5.4: Left: Fraction of Sculptor RGB stars and MW contaminants with respect to the total as function of elliptical radius, derived from the observed surface brightness profile and foreground density in Chapter 4. Right: as before, but these are the expected fractions within the velocity range used for the 3-σ membership selection.

$r < r_2$), and r_1 and r_2 are a generic inner and outer radii defining one elliptical annulus (bin). Figure 5.4 (left) shows that already at a distance of $r \sim$0.7 deg the MW foreground stars outnumber Scl RGB stars.

Line-of-sight velocity distribution of Milky Way stars We use the Besançon model* (Robin et al. 2003) to estimate the velocity distribution of MW stars along the Scl l.o.s. with V magnitude and $V-I$ colour falling within our selection box for RGB stars. The resulting velocity distribution is well approximated by the sum of two Gaussians (see Fig. 5.5):

$$N_{\rm MW,Bes}(v) = k_{1,\rm MW} e^{-\frac{(v-\overline{v}_{1,\rm MW})^2}{2\sigma^2_{1,\rm MW}}} + k_{2,\rm MW} e^{-\frac{(v-\overline{v}_{2,\rm MW})^2}{2\sigma^2_{2,\rm MW}}}. \qquad (5.1)$$

In the heliocentric system the best-fitting parameters are $\overline{v}_{1,\rm MW} = 5.35$ km s^{-1}, $\overline{v}_{2,\rm MW} = 15.98$ km s^{-1}, $\sigma_{1,\rm MW} = 12.86$ km s^{-1}, $\sigma_{2,\rm MW} = 50.37$ km s^{-1} (reduced $\chi^2_{\rm min} = 1.13$). The ratio of the two Gaussians' amplitudes is $R = k_{2,\rm MW}/k_{1,\rm MW} = 1.02$.

We make the reasonable assumption that the shape of the MW velocity distribution does not vary across the small area under consideration. This implies that the parameters $\overline{v}_{1,\rm MW}, \overline{v}_{2,\rm MW}, \sigma_{1,\rm MW}, \sigma_{2,\rm MW}, R$ are fixed. Instead we let the normalization, $k_{1,\rm MW}$ and $k_{2,\rm MW}$, change with the distance from the centre. The reason is that, although the density of MW stars is constant everywhere, the number of MW stars is changing with radius because of the varying area of the elliptical annuli used for the binning.

* http://www.obs-besancon.fr/modele/modele.html

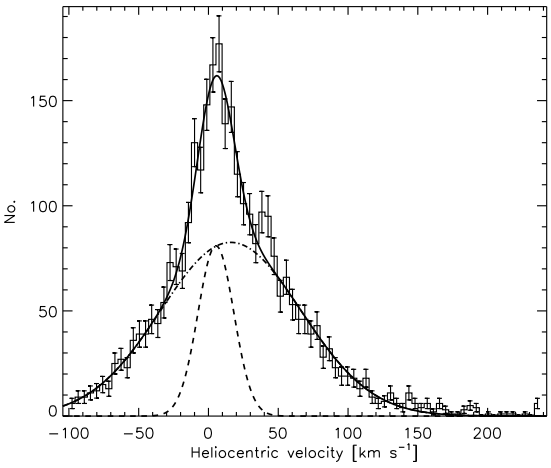

Figure 5.5: Histogram of the velocity distribution of MW stars along the Scl l.o.s. and with V magnitude and $V-I$ colour falling within our RGB selection box from the Besançon model. The errorbars are from Poisson noise. The solid line shows the best-fitting sum of two Gaussian functions, and the dashed and dashed-dotted lines show the individual Gaussians. For our purposes it is important to model the velocity range around [80, 140] km s^{-1}, where Scl stars are likely to be found.

The MW foreground velocity distribution as a function of radius is then:

$$\begin{aligned} N_{\rm MW}(v, r_1 < r < r_2) &= k_{1,\rm MW}(r_1 < r < r_2) e^{-\frac{(v-\overline{v}_{1,\rm MW})^2}{2\sigma^2_{1,\rm MW}}} + \\ &+ k_{2,\rm MW}(r_1 < r < r_2) e^{-\frac{(v-\overline{v}_{2,\rm MW})^2}{2\sigma^2_{2,\rm MW}}}. \end{aligned} \tag{5.2}$$

The number of stars in each elliptical annuli is equal to the integral over the l.o.s. velocities

$$N_{\rm MW}(r_1 < r < r_2) = k_{1,\rm MW}(r_1 < r < r_2)\sqrt{2\pi}\sigma_{\rm eff,MW} \tag{5.3}$$

where we defined $\sigma_{\rm eff,MW} = \sigma_{1,\rm MW} + R\sigma_{2,\rm MW}$. From the above we can derive $k_{1,\rm MW}(r_1 < r < r_2)$ and $k_{2,\rm MW}(r_1 < r < r_2)$:

$$k_{1,\rm MW}(r_1 < r < r_2) = \frac{N_{\rm MW}(r_1 < r < r_2)}{\sqrt{2\pi}\sigma_{\rm eff,MW}} \tag{5.4}$$

and

$$k_{2,\rm MW}(r_1 < r < r_2) = \frac{R N_{\rm MW}(r_1 < r < r_2)}{\sqrt{2\pi}\sigma_{\rm eff,MW}}. \tag{5.5}$$

where $N_{\rm MW}(r_1 < r < r_2)$ is derived from the photometry as described before. Now both the shape and the normalization of the MW foreground l.o.s. velocity distribution are determined at every radius.

dSph velocity distribution We assume that the l.o.s. velocity distribution of the stars in the dwarf galaxy is well described by a Gaussian. At every radius the velocity distribution of the dSph is

$$N_{\rm dSph}(v, r) = \frac{N_{\rm dSph}(r)}{\sqrt{2\pi\sigma^2_{\rm dSph}(r)}} e^{-\frac{(v-\overline{v}_{\rm dSph}(r))^2}{2\sigma^2_{\rm dSph}(r)}} \tag{5.6}$$

where $N_{\rm dSph}(r)$ is fixed by the photometry. The quantity we are interested in is $\sigma_{\rm dSph}(r)$.

Overall probability distribution The probability of observing a velocity v_i extracted from the overall velocity distribution (dSph+MW), taking into account the measured velocity errors σ_i, is:

$$P(v_i \mid \overline{v}_{\rm dSph}, \sigma_{\rm dSph}) = \frac{N_{\rm MW}}{N_{\rm TOT}\sqrt{2\pi}\sigma_{\rm eff,MW}} e^{-\frac{(v_i-\overline{v}_{1,\rm MW})^2}{2\sigma^2_{1,\rm MW}}} + \\ + \frac{RN_{\rm MW}}{N_{\rm TOT}\sqrt{2\pi}\sigma_{\rm eff,MW}} e^{-\frac{(v_i-\overline{v}_{2,\rm MW})^2}{2\sigma^2_{2,\rm MW}}} + \frac{N_{\rm dSph}}{N_{\rm TOT}\sqrt{2\pi(\sigma^2_{\rm dSph}+\sigma^2_i)}} e^{-\frac{(v_i-\overline{v}_{\rm dSph})^2}{2(\sigma^2_{\rm dSph}+\sigma^2_i)}} \quad (5.7)$$

The likelihood of observing a set of velocities v_i with $i = 1, ..., N$ is

$$L(v_1, ..., v_N \mid \overline{v}_{\rm dSph}, \sigma_{\rm dSph}) = \prod_{i=1}^{N} P(v_i) \quad (5.8)$$

We maximize the above likelihood function in each distance bin and find the corresponding best-fitting average velocity $\overline{v}_{\rm dSph}(r)$ and dispersion $\sigma_{\rm dSph}(r)$. The errors are determined from the intervals corresponding to 68.3% probability.

Results: Observed l.o.s. velocity dispersion profile Figure 5.4 (right) shows that only beyond $r \sim 1.3$ deg half of the stars that fall within the velocity range used for the 3σ membership selection are likely to be MW contaminants. This distance corresponds to our last measured point, thus we see that the MW contamination in Scl is not severe in the sampled region. Hence we can use it as a good test for our statistical method which should give similar results to our 3σ selection.

We apply the statistical procedure to the rotation-subtracted GSR velocities. Figure 5.3c,d shows that both the fitted average velocity and dispersion per bin are very similar for the statistical and 3σ determinations. The two profiles are everywhere consistent at the 1σ level. *In the following we will use for our analysis the dispersion profile derived from the maximum likelihood procedure.*

Results: Observed l.o.s. velocity dispersion profile for MR and MP stars We now derive the velocity dispersion profile for MR and MP RGB stars in the Scl dSph. To apply the statistical method that we just described we need to derive: 1) the number profile of MR and MP stars; 2) the amount of foreground contamination in these two populations.

1) In Sect. 4.3.2 we fitted the RGB distribution with two components, where the MR component was represented by a Sersic profile with best-fitting shape parameters (R_s and m) as for the RHB star distribution and the MP component by a Plummer profile with the best-fitting b parameter as for the BHB star distribution. We adopt the normalization found from the two component fit. Therefore we associate to the MR stars a Sersic profile with $I_{0,\rm MR} = 4.5 \pm 0.7$ stars arcmin^{-2}, $R_s = 7.7 \pm 0.9$

arcmin and $m = 0.74 \pm 0.07$, and to the MP stars a Plummer profile with parameters $I_{0,\mathrm{MP}} = 0.60 \pm 0.04$ star arcmin^{-2} and $b_{\mathrm{MP}} = 15.1 \pm 0.5$ arcmin.

2) We need to determine which fraction of the MW foreground contamination derived from the Besançon model might contaminate the MR and the MP Scl components, when considered separately. To estimate this, we simply calculate how many of the stars found in our sample at $v < v_{sys} - 3\sigma$ (i.e. in the non-membership region more populated by foreground stars) are classified as MR ([Fe/H]> -1.5) and how many as MP ([Fe/H]< -1.7), and we repeat this for the various distance bins. The fraction of stars with $v < v_{sys} - 3\sigma$ classified as MR is ~ 0.5, whilst the fraction of stars classified as MP is ~ 0.2. We thus adopt as MW contaminants for the MR and MP population the 50% and 20% of the amount derived from the Besançon model, respectively. Note that as explained in Chapter 4 we are excluding the region $-1.7 <$ [Fe/H] < -1.5 to avoid that the MR and MP components might contaminate each others kinematics.

The resulting velocity dispersion profile for MR stars is shown in Fig. 5.6. The profile declines very fast, and at $r \gtrsim 0.5$ deg the statistical procedure assigns every observed star to the MW component and not to Scl. For comparison the profile resulting from the 3σ selection (also in Fig. 5.6) is very similar to the above profile out to $r \sim 0.5$ deg, whilst at larger distances it gives a higher dispersion, which does not follow the trend observed at smaller radii.

Figure 5.7 shows the velocity dispersion profile for the MP stars, which is consistent with being constant or mildly declining. The shape is very similar to the overall profile derived not imposing any metallicity cut, except at $r \lesssim 0.3$ deg, where the MP velocity dispersion is larger. At those radii the MR stars are present in a considerable number and they tend to lower the overall profile because of their colder kinematics. Note that for the MP stars the contamination from the MW is negligible at all distances.

5.4 Predicted velocity dispersion profile using the Jeans equation

The Jeans equation for a spherical system is

$$\frac{d(\rho_* \langle v_{r,*}^2 \rangle)}{dr} + \frac{\rho_*}{r}[2\langle v_{r,*}^2 \rangle - \langle v_{\theta,*}^2 \rangle - \langle v_{\varphi,*}^2 \rangle] = -\rho_* \frac{d\phi}{dr} = -\frac{V_{\mathrm{c}}^2}{r} \tag{5.9}$$

where ρ_* is the density of the tracer*, $\langle v_{r,*}^2 \rangle$, $\langle v_{\theta,*}^2 \rangle$ and $\langle v_{\varphi,*}^2 \rangle$ are the tracer second velocity moments in the (r, θ, φ) direction respectively, and ϕ and V_{c} are the potential and the circular velocity of the total mass distribution. As described in Binney & Tremaine (1987), let us consider a galaxy whose velocity structure is invariant under rotation about its centre, hence $\langle v_{\theta,*}^2 \rangle = \langle v_{\varphi,*}^2 \rangle$. In the absence of net streaming motions in any of the directions, $\langle v_{r,*}^2 \rangle = \sigma_r^2, \langle v_{\theta,*}^2 \rangle = \sigma_\theta^2, \langle v_{\varphi,*}^2 \rangle = \sigma_\varphi^2$. The Jeans equation thus becomes

$$\frac{1}{\rho_*} \frac{d(\rho_* \sigma_{r,*}^2)}{dr} + \frac{2\beta\sigma_{r,*}^2}{r} = -\frac{d\phi}{dr} = -\frac{V_{\mathrm{c}}^2}{r} \tag{5.10}$$

* By "tracer population" we mean those objects whose kinematics can be used to recover properties of the total potential. In this case our tracers are the stars, which trace the total potential given by the mass distribution of the stars themselves and the DM.

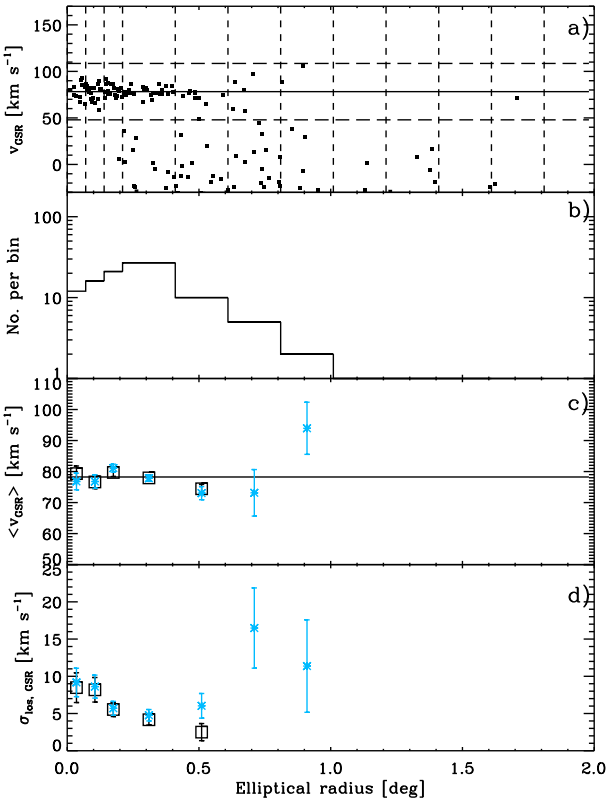

Figure 5.6: Kinematic properties for MR stars ([Fe/H]> -1.5). We show the variation of rotation-subtracted GSR velocity versus elliptical radius (a); number of stars (b); average rotation-subtracted GSR velocity (c); velocity dispersion profile using rotation-subtracted GSR velocities (d). The solid horizontal line indicates the systemic velocity, the horizontal long-dashed lines show the region used for the 3σ membership selection and the vertical dashed lines show the binning. In panel (c) and (d) the squares show the properties which we will use in our analysis and that were derived using the maximum likelihood procedure, whilst the asterisks show the properties derived using the 3-σ clipping. Here we have used a Sersic profile to represent the Scl MR stars in the maximum likelihood procedure for deriving the velocity dispersion. At $r \gtrsim 0.6$ deg the maximum likelihood procedure assigns all the observed stars to the MW component.

where β is the velocity anisotropy parameter, defined as $\beta = 1 - \sigma_\theta^2/\sigma_r^2$, assuming $\sigma_\theta^2 = \sigma_\phi^2$. Note that $\beta = 0$ if the velocity ellipsoid is isotropic, $\beta = 1$ if the ellipsoid is completely aligned with the radial direction, and $\beta < 0$ for tangentially anisotropic ellipsoids.

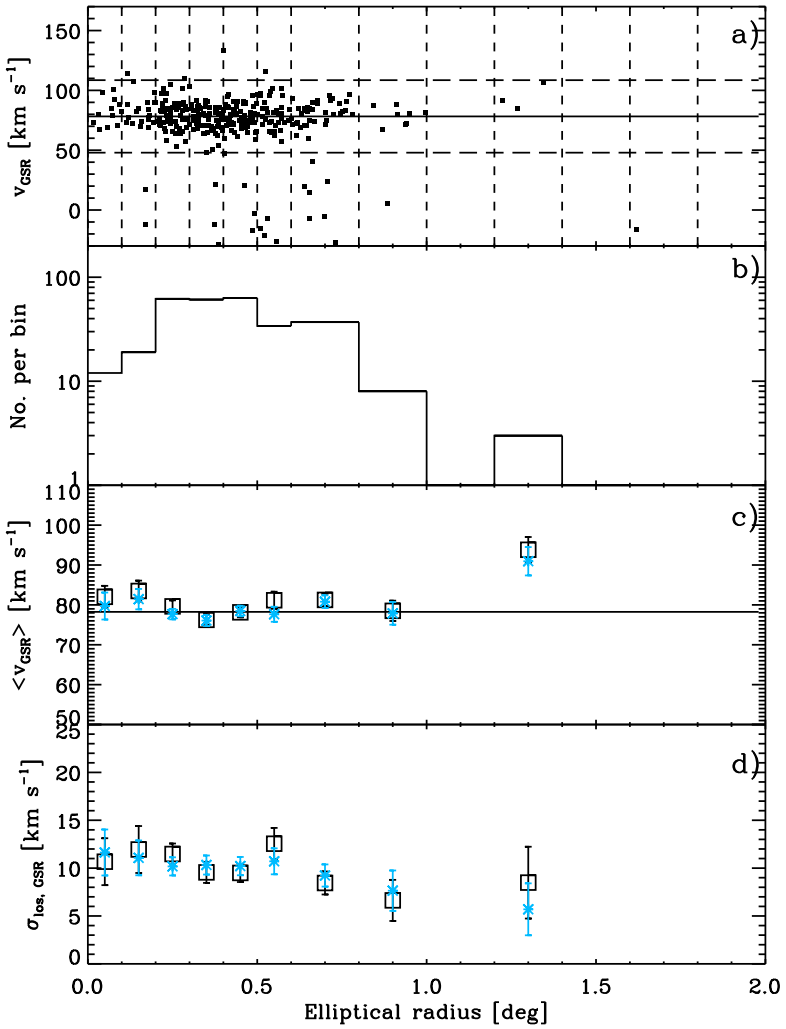

Figure 5.7: As previous figure but for MP stars ([Fe/H]< -1.7). For our analysis we use the dispersion profile derived from the maximum likelihood procedure (squares) for the MP stars.

The Jeans equation relates observable quantities like the density distribution of the tracer and its radial velocity dispersion profile to quantities of interest such as the total mass distribution. Knowing $\rho_*(r)$ and $\beta(r)$, and assuming a mass model, one can derive the predicted radial velocity dispersion profile for the mass model under

consideration and compare it to the observed radial velocity dispersion profile of the tracer. However, knowledge of the velocity anisotropy parameter requires proper motion measurements of the individual stars and at the moment this is possible only in the Solar Neighbourhood. Therefore in practise one uses parametrizations for how β varies with r. The general solution of Eq. 5.10 is

$$\sigma^2_{r,*}(r) = \frac{1}{\rho_* \, e^{\int 2\beta dx}} \int_x^\infty \rho_* \, V_c^2 \, e^{\int 2\beta dx''} \, dx', \qquad x = \ln r. \tag{5.11}$$

The quantity to compare to the observations is the l.o.s. velocity dispersion of the tracer population (Binney & Mamon 1982):

$$\sigma^2_{\rm los}(R) = \frac{2}{\Sigma_*(R)} \int_R^\infty \frac{\rho_*(r)\sigma^2_{r,*} \, r}{\sqrt{r^2 - R^2}} (1 - \beta \frac{R^2}{r^2}) dr \tag{5.12}$$

where R is the projected radius (on the sky) and $\Sigma_*(R)$ is the mass surface density of the tracer.

One common assumption is to treat the velocity anisotropy as constant. In this case the radial velocity dispersion predicted from the Jeans equation for a spherical, non-rotating system is:

$$\sigma^2_{r,*}(\beta = constant) = \frac{r^{-2\beta}}{\rho_*(r)} \int_r^\infty r'^{2\beta} \rho_*(r') \frac{V_c(r')^2}{r'} dr' \tag{5.13}$$

and according to Łokas & Mamon (2003) Eq. 5.12 can be reduced to:

$$\sigma^2_{\rm los}(R) = \frac{2}{\Sigma_*(R)} \int_R^\infty V_c^2(y) y^{2\beta - 1} \rho_*(y) H(y) dy \tag{5.14}$$

with

$$H(y) = \int_R^y (1 - \beta \frac{R^2}{r'^2}) \frac{r'^{\,1-2\beta}}{\sqrt{r'^2 - R^2}} dr'. \tag{5.15}$$

We refer to Mamon & Łokas (2005) for the derivation of the l.o.s. velocity dispersion profile from the Jeans equation using different hypotheses on β.

Although previous studies of dSphs have shown that the luminous matter gravitational contribution is negligible, we can investigate this further by separating $\sigma_{\rm los}$ into the relative contributions of DM and luminous matter, $\sigma^2_{\rm los} = \sigma^2_{\rm los,DM} + \sigma^2_{\rm los,lum}$. These are simply obtained by replacing the circular velocity $V_c^2(r)$ in Eq. 5.14 with $V_c^2(r) = V^2_{\rm c,DM}(r) + V^2_{\rm c,lum}(r)$. dSphs do not appear to contain gas, hence the luminous matter is solely represented by the stars.

As the discovery of multiple stellar populations in dSphs is a recent one, traditionally dSph galaxies have been treated as single component systems. For consistency with previous works, we will first analyze our data using this approach and thus compare the l.o.s. velocity dispersion profile predicted by different DM models to the overall observed l.o.s. dispersion profile. However, we will show that there is a significant advantage in modeling each component (e.g., MR and MP) separately, as it allows us to relieve some of the degeneracies present in the single component modeling.

Below we discuss in detail the ingredients to solve the Jeans equation.

5.4.1 The spatial distribution of the tracer

As a first approach we treat Sculptor as a single component galaxy, i.e. we not make any distinction according to metallicity. In Sect. 4.3.2 we found that the surface number density profile of RGB stars in Scl, $N_*(R)$, is reasonably described by a Plummer profile, with $b = 12.7$ arcmin. Assuming a constant mass-to-light ratio $(M/L)_*$ for the tracer, the surface mass density $\Sigma_*(R)$ is directly related to the surface brightness $I_*(R)$, i.e. $\Sigma_*(R) = (M/L)_* I_*(R)$. We also assume that the surface brightness is directly proportional to the surface number density profile, i.e. $I_*(R) = k\, N_*(R)$ (derived in Sect. 4.3.2). The 3D density profile is derived from $N_*(R)$ through inversion of Abel integrals, assuming that the stars are spherically distributed.

Note that the predicted l.o.s. velocity dispersion profile depends only on the functional form of the spatial distribution of the tracer population, therefore there is no need to set the normalization, i.e. $(M/L)_*$ and k.

In the second approach we treat the MR and MP stars in Scl as distinct tracers. For these we use the Sersic and Plummer profiles from Sect. 5.3.2. For the expression of the 3D density associated to the Sersic profile we refer to Łokas (2002).

5.4.2 The kinematics of the tracer

We examine two specific aspects of the velocity behaviour of the tracer population, namely how to deal with the detected rotation signal and what to assume for the velocity anisotropy parameter.

Rotation: The expression for the projected velocity dispersion (Eq. 5.12), which measures the projected random motion in a galaxy, has been derived for the hypothesis that the system is not rotating.

Observations of rotating elliptical galaxies show that the l.o.s. velocity distribution (LOSVD) is sometimes significantly skewed, so that the observed projected streaming velocity and dispersion are not meaningful. In most of these cases this is due to the presence of an embedded rotating disk (see Binney & Merrifield 1998, and references therein), and the LOSVD can be approximated by a broad non-rotating component superimposed on a narrower rotating component. However, if the LOSVD is close to Gaussian, then the velocity dispersion calculated with respect to the observed streaming motion reflects the intrinsic random motions of the galaxy.

The LOSVD is most likely to be skewed in the regions where the maximum rotation signal is present. We checked that the Sculptor LOSVD in those regions (see Chapter 4) is symmetric and centered around the expected rotation signal. Hence, we can approximate the velocity dispersion derived from the rotation-subtracted velocities with the velocity dispersion predicted for a non-rotating system.

Alternatively, in systems where the rotation law can be accurately derived and there is enough statistics to derive the dispersion profile along both the major and minor axes, one can use the Jeans equations in cylindrical coordinates for a rotating system making an assumption as to how the motion in the azimuthal direction is divided between random motions and streaming motions. The present coverage of this dataset does not allow this alternative.

Velocity anisotropy: As already mentioned, the variation of the velocity anisotropy with radius is not known. We thus compare our observations to the model predictions

for two hypotheses: considering β as constant with radius; using the Osipkov-Merritt parametrization for β (Osipkov 1979; Merritt 1985)

$$\beta_{\rm OM} = r^2/(r^2 + r_a^2) \tag{5.16}$$

where r_a is the anisotropy radius. In the Osipkov-Merritt parametrization the anisotropy is always ≥ 0, i.e. it is never tangential. The central regions are isotropic, and for $r_a \to \infty$ the anisotropy becomes purely radial. At $r = r_a$, $\beta = 0.5$. The smaller r_a, the faster the anisotropy becomes very radial. Models with large r_a correspond to models with almost isotropic behaviour.

5.4.3 Total mass distribution

The total mass distribution in which the tracer population is embedded is given by the contribution of stars and DM.

Stars

To determine the contribution from the luminous matter to the circular velocity, $V_{\rm c,lum}$, we need to know its mass distribution, i.e. $M_{\rm lum}(r)$. What we measure, however, is the number surface density in terms of star counts as a function of the projected radius R. As previously described, we trasform this into a surface brightness, $I_{\rm lum}(R)$, and then into a mass surface density, $\Sigma_{\rm lum}(R)$. If we assume that the stellar population is homogeneusly distributed with r, then the surface brightness profile $I_{\rm lum}(R)$ is proportional to the number surface density profile. The surface density is then $\Sigma_{\rm lum}(R) = (M/L)_{*,\rm V}\ I_{\rm lum}(R)$.

From our photometric analysis we found that the projected distribution of all Scl stars (from the 90% complete sample) is best approximated by a Plummer profile with $b = 13.1 \pm 0.2$ arcmin. This is also consistent with the best-fitting profile for the tracer population, i.e. the RGB stars. The mass distribution for a Plummer profile is

$$M_{\rm lum}(r) = \frac{(M/L)_{\rm lum}\, L_{\rm tot}\, r^3}{(b^2 + r^2)^{3/2}} \tag{5.17}$$

where $(M/L)_{\rm lum}$ is the mass-to-light ratio of the luminous component and $L_{\rm tot}$ its luminosity.

We assume $L_{\rm tot} = L_{*,\rm V} = 2.15 \times 10^6 L_\odot$ (Mateo 1998) and $(M/L)_{lum,V}$ =2. The sole effect of the mass-to-light ratio is to vary the amplitude of the projected velocity dispersion for the luminous component as $\sqrt{(M/L)_{*,V}}$. We will see in the next section that the contribution of the luminous matter to the total dispersion is negligible for any reasonable choice of $(M/L)_{lum,V}$.

Dark matter

We consider two different models for a spherically symmetric dark-matter halo potential:

- *Pseudo-Isothermal sphere.* This model has been extensively used in the context of extragalactic rotation curve work (see Swaters et al. 2000, and references therein). The density profile and circular velocity associated to this model are:

$$\rho(r) = \rho_0 \frac{r_\mathrm{c}^2}{(r_\mathrm{c}^2 + r^2)}, \tag{5.18}$$

and

$$V_\mathrm{c}^2(r) = V_\mathrm{c}^2(\infty)\big(1 - \frac{r_\mathrm{c}}{r} \arctan \frac{r}{r_\mathrm{c}}\big), \tag{5.19}$$

where r_c is the core radius, $\rho_0 = \dfrac{V_\mathrm{c}^2(\infty)}{4\pi G r_\mathrm{c}^2}$ is the central density and $V_\mathrm{c}(\infty)$ is the asymptotic circular velocity. At large radii the density behaves as $\rho \propto r^{-2}$.

The resulting mass profile is:

$$M(< r) = 4\pi\rho_0 r_\mathrm{c}^2\big(r - r_\mathrm{c} \arctan \frac{r}{r_\mathrm{c}}\big). \tag{5.20}$$

The profile is completely defined by ρ_0 and r_c, or any couple of non-degenerate parameters.

- *NFW model.* This profile is motivated by cosmological N-body simulations in a CDM framework (Navarro et al. 1996, 1997). In this case the DM density profile is given by

$$\rho(r) = \frac{\delta_c \rho_\mathrm{c}^0}{(r/r_\mathrm{s})(1 + r/r_\mathrm{s})^2} \tag{5.21}$$

where r_s is a scale radius, ρ_c^0 the present critical density and δ_c a characteristic over-density. The latter is defined by $\delta_\mathrm{c} = \dfrac{100\, c^3 g(c)}{3}$, where $c = r_\mathrm{v}/r_\mathrm{s}$ is the concentration parameter of the halo, r_v its virial radius, and $g(c) = (\ln(1+c) - c/(1+c))^{-1}$. The circular velocity associated with this density distribution is

$$V_\mathrm{c}^2(s) = \frac{V_\mathrm{v}^2 g(c)}{s}\left[\ln(1 + cs) - \frac{cs}{1 + cs}\right] \tag{5.22}$$

where V_v is the circular velocity at the virial radius r_v and $s = r/r_\mathrm{v}$. The concentration c has been found to correlate with the halo virial mass M_v in the range 10^{11}-$10^{14} h^{-1}\ M_\odot$ (Navarro et al. 1997; Bullock et al. 2001; Wechsler et al. 2002), so that at a given redshift more massive haloes have lower concentrations. Using the formula in Gentile et al. (2007) the concentration predicted for a MW-sized halo ($M_\mathrm{V} \sim 1.0 \times 10^{12}\ M_\odot$) is ~ 10; extrapolating the behaviour at smaller masses, higher concentrations are expected for dSph galaxies ($c = 20$ for a virial mass $\sim 10^{10}\ M_\odot$ and $c = 35$ for a virial mass $\sim 10^8\ M_\odot$). In principle, the relation between c and M_v makes the NFW model completely defined by one parameter (e.g., M_v). However at a fixed mass the scatter in the predicted concentration is large, of the order of $\Delta(\log_{10} c) = 0.18$ (Bullock et al. 2001), thus we do not consider the NFW density profile as a one-parameter family, but

we describe it both by the concentration c and by the virial mass or the circular velocity at the virial radius.

At large radii (for $r \gg r_{\rm s}$), the density behaves as $\rho \propto r^{-3}$, and therefore, the total mass diverges logarithmically. The resulting mass profile is

$$M(<r) = M_v \, \frac{f(r/r_s)}{f(c)} \tag{5.23}$$

where $f(x) = \ln(1+x) - \dfrac{x}{1+x}$

When integrating Eq. 5.12, we set the upper integration limit to $r_{\rm v}$ where we use $r^{2\beta}\rho_* \sigma^2_{r,*}|_{r_{\rm v}} = 0$ (we are essentially assuming that the particles are bound out to the virial radius). As we will see in the next Section, the extent of the luminous matter is a few kpc, an order of magnitude smaller than the extent of the DM halo, thus setting the upper integration limit to $r_{\rm v}$ instead of to infinity will not affect our results, only decrease the computation time.

5.5 Results from kinematic modeling

The methodology we use consists of comparing the observed l.o.s. velocity dispersion $\sigma_{\rm los}$ for each distance bin with that predicted for the different models discussed in the Sect. 5.4. We explore the space of parameters which define each model and determine the χ^2 as:

$$\chi^2 = \sum_{i=1}^{Nbins} \left(\frac{\sigma_{{\rm los}_i} - \sigma_{\rm los}(R_i; p_\beta, p)}{\epsilon_i} \right)^2 . \tag{5.24}$$

The variable p denotes a characteristic parameter of each dark matter model (e.g. the mass enclosed within the last measured point for the isothermal sphere and the virial mass for the NFW model), p_β denotes a parameter describing the behaviour of the velocity anisotropy ($p_\beta = \beta$ for the models using β constant with radius, $p_\beta = r_a$ for the models using $\beta_{\rm OM}$). Finally, ϵ_i is the error in the observed l.o.s. velocity dispersion. The best-fitting parameters are defined as those for which χ^2 is minimized. We quote as errors in the individual parameters the projections of the $\Delta\chi^2 = 2.3$ region (corresponding to the region of 68.3% *joint* probability for a two free parameters χ^2 distribution).

5.5.1 Scl as a single component galaxy

β constant with radius

- **Isothermal sphere:** In this model the total mass of the DM halo is not finite, therefore we choose to fit the value of the mass within the last measured point, $M(<r_{\rm last})$, where $r_{\rm last}$ =1.8 kpc. This quantity is related to the core radius and the asymptotic circular velocity by $V_{\rm c}^2(\infty) = G\,M(<r_{\rm last}) \left(r_{\rm last} - r_c \arctan \dfrac{r_{\rm last}}{r_c} \right)^{-1}$.

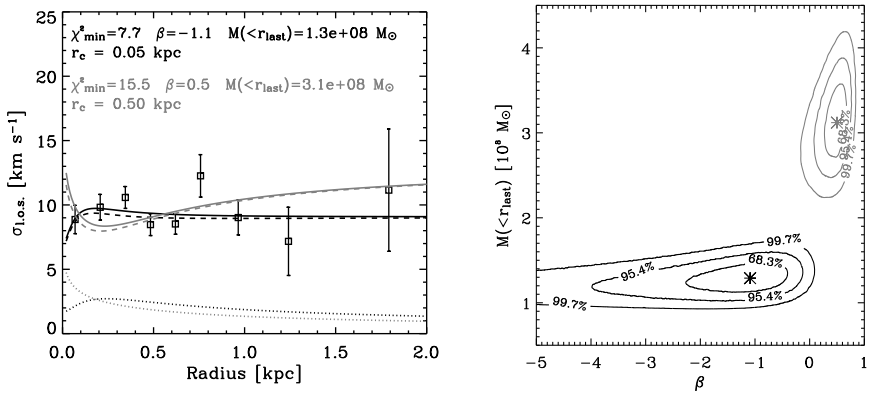

Figure 5.8: Left: Observed l.o.s. velocity dispersion profile (squares with errorbars) overlaid on the best fit model (solid line) for an **isothermal sphere with β constant** and $r_c = 0.05$ (black), 0.5 kpc (grey). The dotted lines show the contribution of the stars (M/L=2) and the dashed lines the dark matter contribution. Assuming a distance of 79 kpc for the Scl dSph, 1 deg $\sim$ 1.4 kpc. Right: Contour plots of $\Delta\chi^2$ corresponding to a probability of the 68.3%, 95.4% and 99.73% (1-2-3σ regions) for the isothermal sphere models shown in the left panels, as indicated by the colours.

Therefore the isothermal sphere model can be fully described by two parameters, i.e. $M(< r_{\rm last})$ and r_c. The other free parameter to take into account is the velocity anisotropy β. In practise, we fix the core radius to several values and minimize the χ^2 to obtain the best-fitting $M(< r_{\rm last})$ and β.

We explore the performance of models with core radii $r_c = 0.001$, 0.05, 0.1, 0.5, 1 kpc (in Fig. 5.8 we plot the results for the $r_c = 0.05, 0.5$ kpc models). We find that the best results are obtained for core radii smaller than 0.1 kpc. The latter models predict similar velocity dispersion profiles, of comparable fit-qualities ($\chi^2_{\rm min} \sim 8$), and result in tangential values of the velocity anisotropy.

This tendency for increasing tangential anisotropy with decreasing core radius comes from the fact that smaller core radii models have higher concentrations of mass in the central regions and this tends to increase the central value of the velocity dispersion. To match a nearly constant velocity dispersion profile the anisotropy then needs to be tangential.

Figure 5.8 show the results for the model with $r_c = 0.05$ kpc, with best-fitting parameters $\beta = -1.1^{+0.7}_{-1.1}$ and $M(< r_{\rm last}) = 1.3 \pm 0.2 \times 10^8\ M_\odot$. In general, we find that as the core radius increases, the best-fitting anisotropy changes from tangential to radial and the best-fitting mass becomes larger. For r_c=0.5 kpc (see Fig. 5.8), the predicted velocity dispersion profile is too large both in the inner and in the outer regions. The ability of the isothermal model to fit these data diminishes for larger core radii.

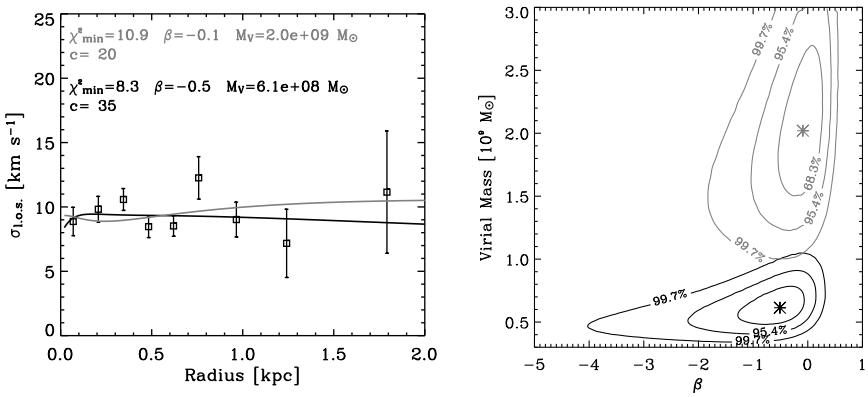

Figure 5.9: Left: Observed l.o.s. velocity dispersion profile (squares with errorbars) overlaid on the best fit models (solid lines) for an **NFW model with β constant** and c=20 (grey), 35 (black). Right: Contour plot of $\Delta\chi^2$ corresponding to a probability of the 68.3%, 95.4% and 99.73% (1-2-3σ regions) for the NFW models shown in the top panel, as indicated by the colours.

- **NFW model:** For this model we let the concentration vary from c =20, 25, 30, 35, and for each of these values we derive the best-fitting virial mass and velocity anisotropy.

  Among the four models we explored, the one with the highest concentration, $c = 35$, gives the best result, with best-fitting parameters $\beta = -0.5^{+0.4}_{-0.8}$ and a virial mass $M_v = 6.1^{+2.2}_{-1.6} \times 10^8\ M_\odot$ ($\chi^2_{\rm min} = 8.3$, $M(< r_{\rm last}) = 1.4^{+0.5}_{-0.4} \times 10^8\ M_\odot$). For the other concentrations the best-fitting profiles are in reasonable agreement with the data ($\chi^2_{\rm min}$ =8.8-10.9). The best-fitting virial mass differs by approximately a factor two between the lowest and highest concentration models (in Fig. 5.9 we plot the results for the $c = 20$ and $c = 35$ models), whilst the best-fitting anisotropies are all mildly tangential, and consistent with each other. We can refer to this effect as to the "virial mass-concentration degeneracy": for each concentration, the combination of c and the best-fitting virial mass is such that all the models have similar $M(r)$ within the last measured point, which in turn results in similar best-fitting β for all of them to be consistent with the same $\sigma_{\rm los}$.

β Osipkov-Merritt

We now relax the assumption of a constant velocity anisotropy. We repeat the fitting procedure using $\beta_{\rm OM}$ for the velocity anisotropy. In this case the anisotropy radius r_a is the free parameter.

- **Isothermal sphere:** we explore the same range of core radii as in the previous section (Fig. 5.10). In this case the best-fitting model is defined by r_c =0.5 kpc, $r_a = 0.4^{+0.2}_{-0.1}$ kpc and $M(< r_{\rm last}) = 3.2 \pm 0.5 \times 10^8\ M_\odot$ ($\chi^2_{\rm min} = 8.3$). Also the

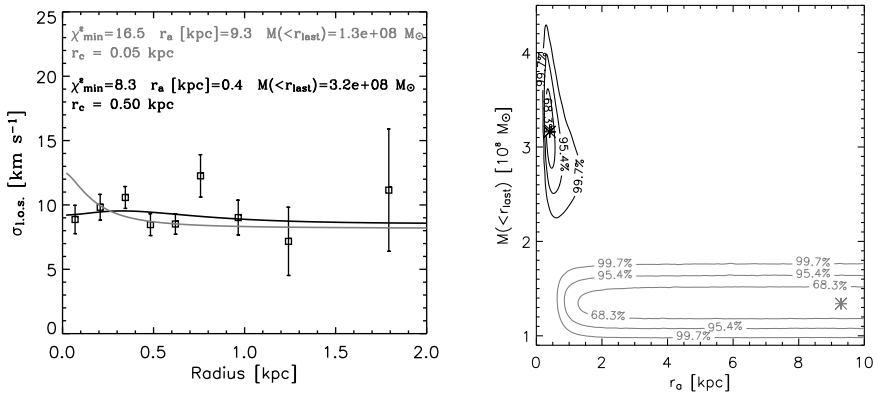

Figure 5.10: As Fig. 5.8. Here the model is an **isothermal sphere with** $\beta_{\rm OM}$; the grey line and contours show the $r_c = 0.05$ kpc model and the black lines and contours the $r_c = 0.5$ kpc model.

models with $r_c = 0.1, 1$ kpc give acceptable results. The resulting best-fitting mass for each of the models is almost equal to the case with constant anisotropy, whilst the quality of the fit is in some cases very different. Now that the minimum value the anisotropy can assume is zero, the predicted central dispersion remains too high for small core radii, resulting in a bad fit. Conversely, for large core radii instead the fit with constant β was predicting too large a dispersion in the outer parts, which is now lowered by the very radial anisotropy, giving an acceptable fit.

- **NFW model:** we explore the same range of concentrations as in the previous section (Fig. 5.11). As in the hypothesis of constant anisotropy, the explored models with different concentrations give similar, acceptable results, with best-fitting masses comparable to the previous case and velocity anisotropies consistent with isotropy. Unlike the constant β case, now the quality of the fit improves for lower concentrations.

Remarks on this section

From the above analysis we see that the modeling of Scl as a single component system is subject to several degeneracies.

The isothermal sphere model gives an example of the well-known "mass profile-anisotropy degeneracy": the best-models for the $\beta(r) = constant$ case, which have small core radii ($r_c < 0.1$ kpc), mildly tangential β and a mass within the last measured point of $\sim 1.3 \times 10^8\ M_\odot$, give fits of comparable quality to the best-model with $\beta(r) = \beta_{\rm OM}$ (i.e. radial anisotropy), which has a larger core radius ($r_c = 0.5$ kpc) and approximately twice the mass. In this case, knowledge of the global value of the anisotropy parameter would help to distinguish between the two models.

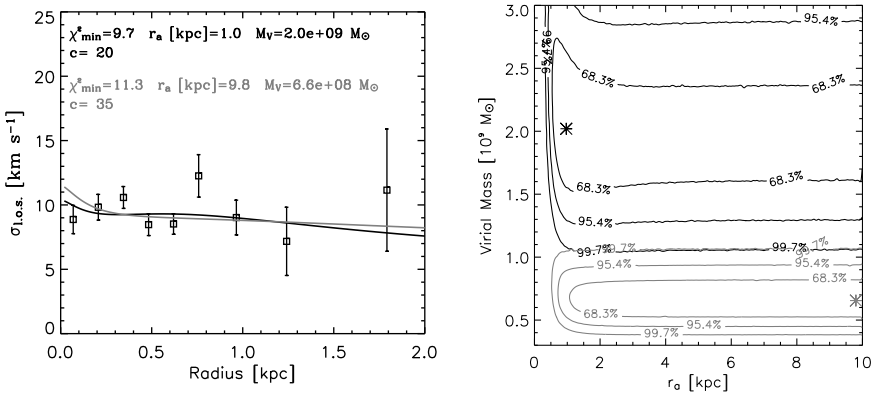

Figure 5.11: As Fig. 5.9. Here the model is an **NFW with** $\beta_{\rm OM}$; the black line and contours show the $c = 20$ model and the grey lines and contours the $c = 35$ model.

Within the $\beta(r) = constant$ case, which is slightly favoured with respect to the $\beta(r) = \beta_{\rm OM}$ case, we find that it is not possible to distinguish between an isothermal sphere and an NFW model. The best isothermal models ($r_c < 0.1$ kpc) produce very similar velocity dispersion profiles to the best NFW model ($c = 35$), both in terms of the mass predicted within the last measured point (1.3-1.4$\times10^8$ $M_\odot$) and of the predicted, mildly tangential, anisotropy. The reason for this is that we are sampling a distance range where the logarithmic slope of the dark matter density distribution is very similar for both the models, explaining the similarities between the two fits.

5.5.2 Scl as a two component galaxy

From the previous section we saw that it is difficult from the analysis of the overall velocity dispersion profile of Scl to prefer one dark matter model over the other. We now use Scl MR and MP components as different tracers of the same potential in the attempt to relieve some of the above degeneracies.

In this case we treat as free parameters: the mass of dark matter in Scl (virial or within the last measured point), the parameter defining the anisotropy of the MR stars ($\beta_{\rm MR}$ or $r_{\rm a,MR}$) and the anisotropy of the MP stars ($\beta_{\rm MP}$ or $r_{\rm a,MP}$) as there is no reason to assume that MR and MP stars have the same orbital chracteristics. For each combination of these 3 parameters we compare the predicted to the observed velocity dispersion for the MR component, obtaining a $\chi^2_{\rm MR}$ value. We repeat this exercise for the MP component ($\chi^2_{\rm MP}$). We find the best-fitting parameters by minimizing the sum $\chi^2 = \chi^2_{\rm MR} + \chi^2_{\rm MP}$. The resulting χ^2 distribution has 3 free parameters and 11 degrees of freedom, and as errors in the individual parameters we quote the projection of the region of *combined* 68.3% probability (corresponding to a $\Delta\chi^2 = 3.53$).

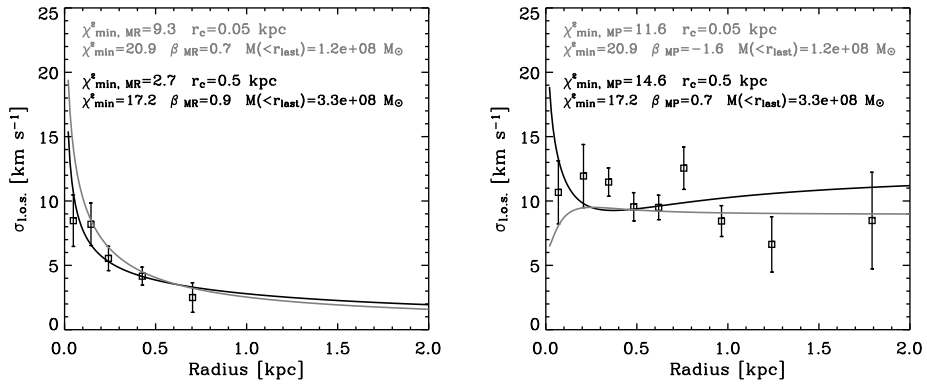

Figure 5.12: Observed MR (left) and MP (right) velocity dispersion profile (squares with errorbars) wih overlaid the best-fitting model (solid line) from the joint fit of the velocity dispersion profile of MR and MP stars. The model is an **isothermal halo**, in the hypothesis of β **constant** with the radius and $r_c = 0.05$ kpc (grey), 0.5 kpc (black).

β constant with radius

In this case the fits for both an isothermal and an NFW model are quite poor, as the joint fits are not satisfactory for both MR and MP components simultaneously.

- **Isothermal sphere:** the best result for a joint fit of the MR and MP velocity dispersion profiles is given by a model with a core radius $r_c = 0.5$ kpc, $M(< r_{\rm last}) = 3.3 \pm 0.8 \times 10^8\ M_\odot$, $\beta_{\rm MR} \gtrsim 0.65$, $0.3 \lesssim \beta_{\rm MP} \lesssim 0.9$, with $\chi^2_{\rm min} = (\chi^2_{\rm MR} + \chi^2_{\rm MP})_{\rm min} = 17.3$ (Figs. 5.12, 5.A1). All the models are able to reproduce the rapid decline of the MR velocity dispersion with very radial anisotropies. In general larger core radii are preferred by the MR population not to overpredict the amplitude of the central dispersion. Instead the almost flat trend of the MP population is better reproduced by small core radii and tangential anisotropy.

- **NFW model:** Figures 5.13 and 5.A2 show that lower concentrations are favoured by the MR component for the same reason as above: the lower concentration models predict a lower central dispersion, because they have less mass in the central regions. As for the isothermal model, very radial anisotropies are required to explain the rapid decline of the MR velocity dispersion. In contrast the MP dispersion is better described by models with larger concentrations and tangential β.

β Osipkov-Merritt

- **Isothermal sphere:** When assuming a $\beta_{\rm OM}$ (Figs. 5.14, 5.A3) we find that an isothermal sphere model with r_c =0.5 kpc, $M(< r_{\rm last}) = 3.4 \pm 0.7 \times 10^8\ M_\odot$, $r_{\rm a,MR} = 0.2^{+0.1}_{-0.15}$ and $r_{\rm a,MP} = 0.4^{+0.3}_{-0.2}$ kpc gives an excellent description of both

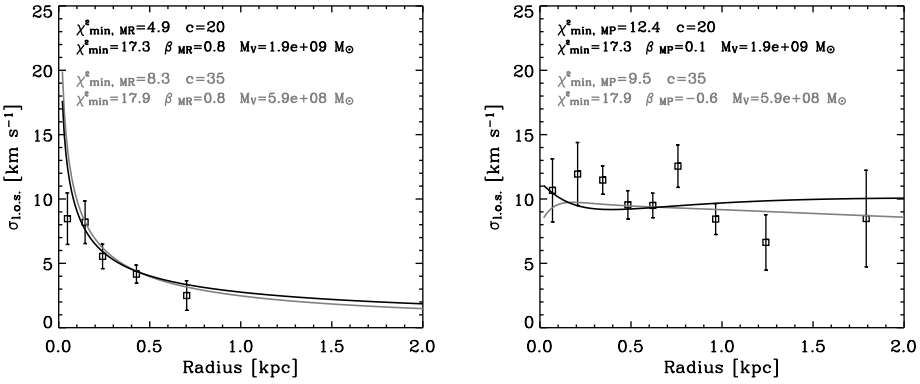

Figure 5.13: Observed MR (left) and MP (right) velocity dispersion profile (squares with errorbars) wih overlaid the best-fitting model (solid line) from the joint fit of the velocity dispersion profile of MR and MP stars. The model is an **NFW halo**, in the hypothesis of β **constant** with the radius and c =20 (black), 35 (grey).

the MR and MP velocity dispersion profiles ($\chi^2_{\rm min} = 6.9$, with $\chi^2_{\rm MR} = 0.6$ and $\chi^2_{\rm MP} = 6.3$).

Models with different core radii yield either a good fit for the MR stars or for the MP stars, but not for both simultaneously.

- **NFW model:** In the case of an NFW halo (Figs. 5.15, 5.A4), the best fit is given by a model with $c = 20$, $M_v = 2.2^{+1.0}_{-0.7} \times 10^9\ M_\odot$, $r_{\rm a,MR} = 0.2 \pm 0.1$ kpc and $r_{\rm a,MP} = 0.8^{+2.0}_{-0.4}$ kpc ($\chi^2_{\rm min} = 10.8$, with $\chi^2_{\rm MR} = 4.2$ and $\chi^2_{\rm MP} = 6.6$). This gives a mass within the last measured point of $\sim 2.4^{+1.1}_{-0.7} \times 10^8\ M_\odot$, which is consistent with the mass predicted by the best-fitting isothermal sphere model. This model tends to overpredict the central values of the MR velocity dispersion, and this tendency is accentuated for larger concentrations. NFW haloes with $c < 20$ would be needed to improve the agreement with the MR dataset. We discuss this further below.

Remarks on this section

The joint fit of the observed velocity dispersion profile for MR and MP stars reveals that both for an isothermal and an NFW model, a constant velocity anisotropy is strongly disfavoured. Models with Osipkov-Merritt velocity anisotropy give excellent fits to the data (see Table 5.1). In both cases the quality of the fit for the MP component is comparable ($\chi^2_{\rm min} \sim 6$). There is however a significant difference in the quality of the fit for the MR component, which is much better for the isothermal sphere. The NFW model, on the other hand, overpredicts the central values of the MR velocity dispersion profile.

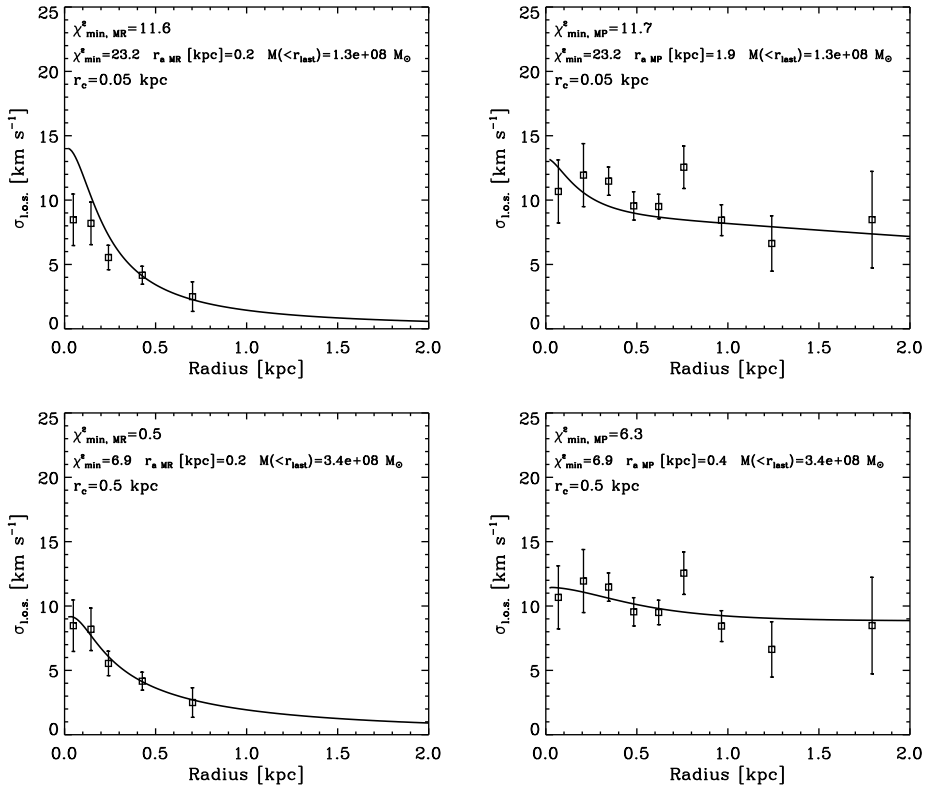

Figure 5.14: Observed MR (left) and MP (right) velocity dispersion profile (squares with errorbars) wih overlaid the best-fitting model (solid line) from the joint fit of the velocity dispersion profile of MR and MP stars. The model is an **isothermal halo**, in the hypothesis of $\beta_{\rm OM}$ and r_c =0.05 kpc (top), 0.5 kpc (bottom).

Table 5.1: Parameters of the best-fitting dark matter models for the two components Sculptor modeling. The columns show: the minimum χ^2, the reduced minimum χ^2, the minimum χ^2 for the MR and the MP component, the parameter defining the anisotropy of the MR and the MP component (this is β itself for the $\beta = const$ case, and the anisotropy radius r_a[kpc] for the $\beta = \beta_{\rm OM}$ case), the mass contained within the last measured point.

	$\chi^2_{\rm min}$	$\chi^2_{\rm min}/\nu$	$\chi^2_{\rm min,MR}$	$\chi^2_{\rm min,MP}$	$p_{\beta,MR}$	$p_{\beta,MP}$	M($< r_{\rm last}$)
Iso $r_c = 0.5$ kpc $\beta = const$	17.3	1.6	2.7	14.6	0.9	0.7	$3.3\pm0.8 \times 10^8\ M_\odot$
NFW $c = 20$ $\beta = const$	17.3	1.6	4.9	12.4	0.8	0.1	$2.0^{+1.3}_{-0.7} \times 10^8\ M_\odot$
Iso $r_c = 0.5$ kpc $\beta = \beta_{\rm OM}$	6.9	0.6	0.5	6.3	0.2	0.4	$3.4\pm0.7 \times 10^8\ M_\odot$
NFW $c = 20$ $\beta = \beta_{\rm OM}$	10.8	1.0	3.8	7.0	0.2	0.8	$2.4^{+1.1}_{-0.7} \times 10^8\ M_\odot$

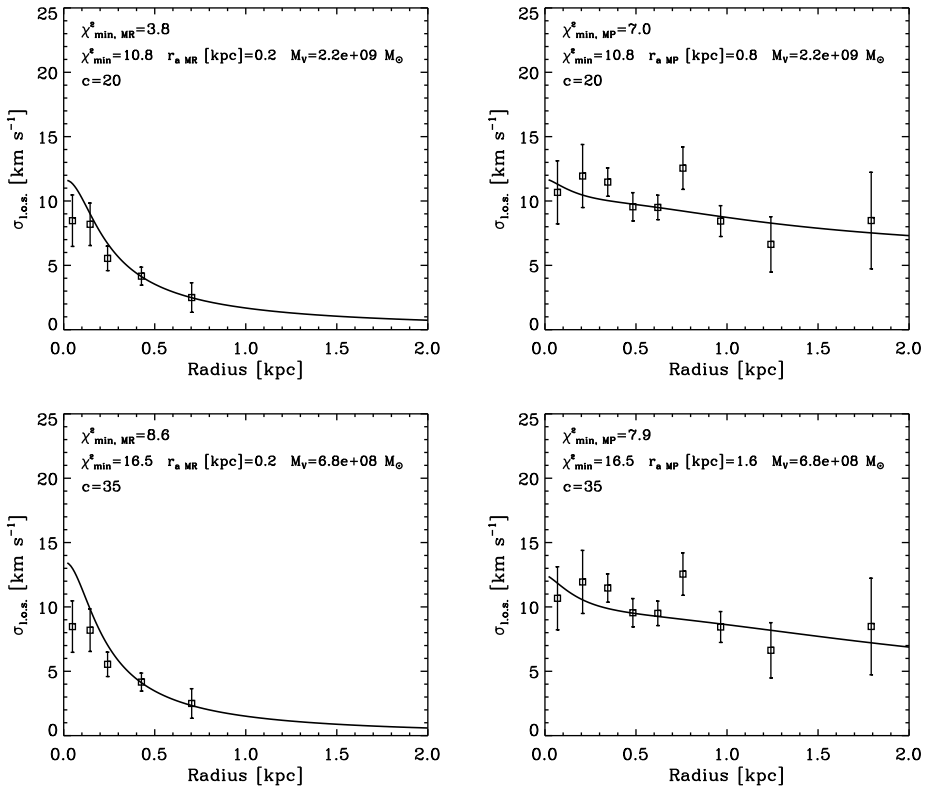

Figure 5.15: Observed MR (left) and MP (right) velocity dispersion profile (squares with errorbars) wih overlaid the best-fitting model (solid line) from the joint fit of the velocity dispersion profile of MR and MP stars. The model is an **NFW halo**, in the hypothesis of $\beta_{\rm OM}$ and c =20 (top), 35 (bottom).

It is particularly important then to accurately determine the amplitude of the central values of the velocity dispersion profile. For this we can use our VLT/FLAMES velocities from high resolution (HR) measurements in the central regions of the Scl dSph. As described in Chapter 2, 93 stars in the Scl central regions overlap in our HR and LR datasets. As the HR velocities are derived from the measurements of ∼100 lines, the resulting error in velocity is considerably smaller than the one we typically obtain from CaT measurement.

The velocity dispersion derived from the HR measurements for MR and MP stars is shown in Fig. 5.16 and agrees well with the dispersion from the CaT. The value of the velocity dispersion for the MR stars using the HR data is $\sim 6.4 \pm 1.1$ km s^{-1} at $R = 0.15$ kpc in comparison to the LR value 8.2±1.7 km s^{-1}. When repeating the χ^2 fitting procedure substituting the velocity dispersion from the LR in the first 3 bins with that obtained from the HR dataset we find that the NFW model fits are worst, even if we allow for lower concentrations. The best fit is now obtained for

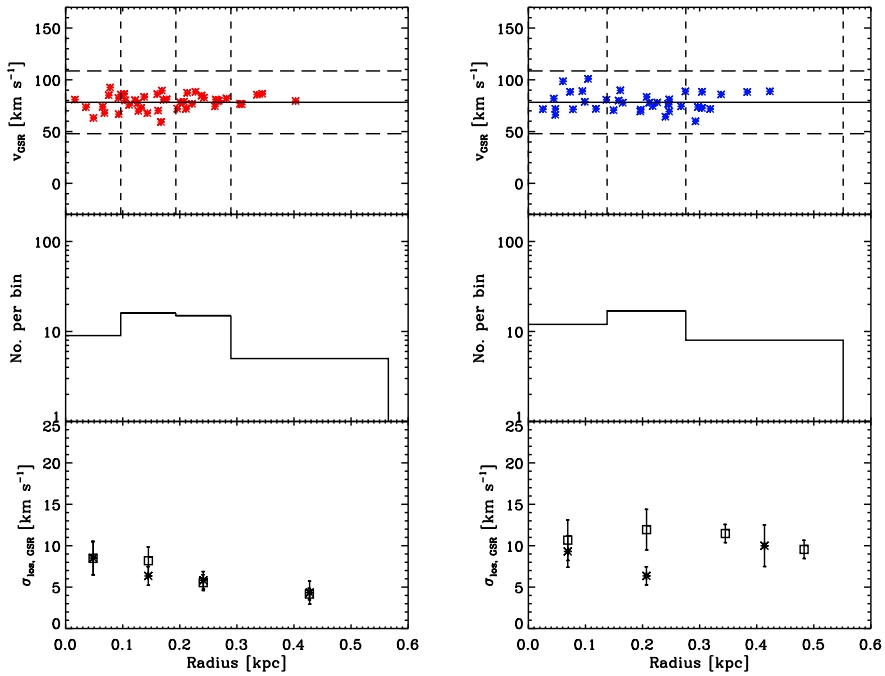

Figure 5.16: HR VLT/FLAMES Scl sample (left: MR stars; right: MP stars). From top to bottom: rotation-subtracted GSR velocity, number of stars per bin, velocity dispersion per bin (asterisks). For comparison the squares with errorbars in the bottom panels show the velocity dispersion for MR (left) and MP (right) stars derived from our low resolution sample. The solid horizontal line indicates the systemic velocity; the dotted lines the usual 3σ range; the vertical dashed lines the binning used.

a $c = 15$ and $M_v = 4.2^{+2.5}_{-1.7} \times 10^9\ M_\odot$ model. This model predicts a lower velocity dispersion for the MR stars, more in agreement with the data, but the overall fit is still not satisfactory for this component ($\chi^2_{\rm min} = 12.7$, $\chi^2_{\rm min,MR} = 4.8$). For higher concentrations the performance of the fit improves for the MP stars and is poorer for the MR, and viceversa for lower concentrations.

On the contrary an isothermal sphere with r_c =0.5 kpc still gives an excellent fit using also the HR data. This further strengthens the case for the isothermal sphere model with relatively large core under the assumption of an Osipkov-Merritt anisotropy.

5.6 MOND

As alternative to the presence of dark matter, we briefly explore the performance of Modified Newtonian Dynamics (MOND) in recovering the observed l.o.s. velocity dispersion profile of Scl. First we consider all Scl members together and then we jointly

fit the dispersion profiles of MR and MP stars.

In the MOND framework the true acceleration $\mathbf{g}$ is related to the Newtonian acceleration $\mathbf{g_N}$ by

$$\mu(x)\mathbf{g} = \mathbf{g_N} \tag{5.25}$$

where $x = |g|/a_0$, a_0 is the critical acceleration and $\mu(x)$ is an unspecified function that asymptotically behaves as $\mu(x) = x$ when $x \ll 1$ and $\mu(x) = 1$ when $x \gg 1$ (Milgrom 1983). The standard value of a_0 was derived by Begeman, Broeils, & Sanders (1991) from a sample of high-resolution rotation curves for spiral galaxies and is $a_0 = 1.2 \times 10^{-10}$ m s^{-2}.

In principle, the attractiveness of MOND resides in its predictive power. Unlike in the case of dark matter models, the MOND potential does not involve free parameters and it is completely defined by a_0 and the amount of visible matter, parametrized by its mass-to-light ratio M/L. The MOND force field is determined through Eq. 5.25. We can use the Jeans equation to derive the predicted MOND l.o.s. velocity dispersion profile where the total potential is represented by the stellar potential in the MOND regime. Now that the only potential is due to the stars we cannot fix the stellar M/L but we must consider it as a free parameter. In this case we use the stellar M/L in the V band. As in the previous section we must assume a functional form for β (with a corresponding free parameter).

For $\mu(x)$ we explore the performance of $\mu_{\rm KM}(x) = x/\sqrt{1+x^2}$ (Kent 1987; Milgrom 1988, hereafter KM), and $\mu_{\rm FM05}(x) = x/(1+x)$, which was found to better agree with observations of the terminal velocity curve of the MW given the standard value of a_0 (Famaey & Binney 2005, hereafter FB05).

The solutions for the gravitational field in the MOND regime are:

$$g_{\rm KM} = a_0 \sqrt{\frac{y^2 + y\sqrt{y^2+4}}{2}} \tag{5.26}$$

and

$$g_{\rm FB05} = \frac{a_0}{2}\left(y + \sqrt{y^2+4y}\right) \tag{5.27}$$

where $y = g_N/a_0$.

5.6.1 Scl as a single component galaxy

In the case of Scl the stars are distributed as a Plummer sphere with $b = 13.1$ arcmin (as in Sect. 5.4.3). We find a good agreement between the predicted l.o.s. velocity dispersion profile and the observed one, both in the case of β constant with radius and $\beta_{\rm OM}$ (reduced $\chi^2_{\rm min} \sim 1$). Both functional forms for $\mu(x)$ give very similar and consistent results for the best-fitting values of the free parameters. The model that performs slightly better has constant β and $\mu_{\rm FM05}$, which gives a $\chi^2_{\rm min} = 8.1$ for a $\beta = -0.3^{+0.3}_{-0.5}$ and M/L$= 4.1^{+1.1}_{-0.8}$ $(\mathrm{M/L})_\odot$ (Fig. 5.17). The predicted shape and quality of fit are very similar to the best-fitting DM models (see Sect. 5.5).

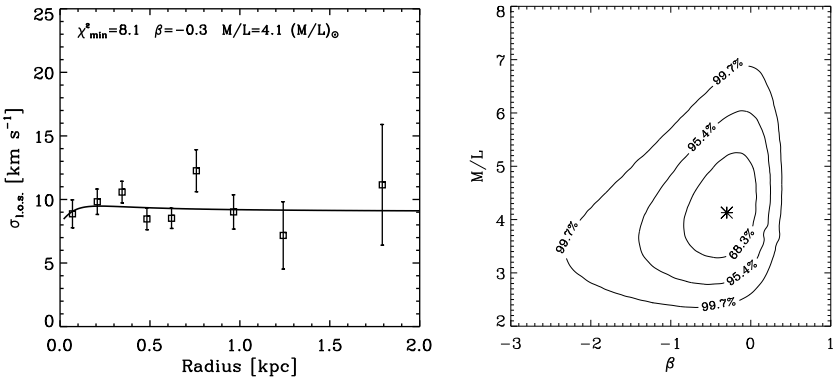

Figure 5.17: Left: Observed velocity dispersion profile for the Sculptor dSph (squares with errorbars) wih overlaid the best-fitting MOND model (solid line) in the hypothesis of β **constant with radius**. Here we use the functional form for $\mu(x)$ proposed by KM (see text). Right: Contour plot of $\Delta\chi^2$ corresponding to a probability of the 68.3%, 95.4% and 99.73% (1-2-3σ regions) relative to the model in the left panel.

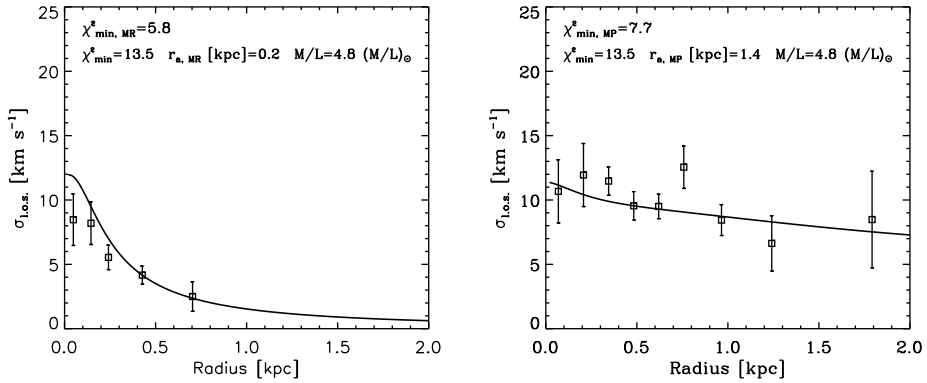

Figure 5.18: Observed MR (left) and MP (right) velocity dispersion profile (squares with errorbars) wih overlaid the best-fitting MOND model (solid line) from the joint fit of the velocity dispersion profile of MR and MP stars in the hypothesis of $\beta_{\rm OM}$. Here we use the functional form for $\mu(x)$ proposed by FM05 (see text).

5.6.2 Scl as a two component galaxy

In the case of a combined fit of the MR and MP velocity dispersion profiles we find that there is a better agreement between predictions and observations in the case of $\beta_{\rm OM}$. The best-fitting model ($\chi^2_{\rm min} = 13.5$, with $\chi^2_{\rm MR} = 5.8$ and $\chi^2_{\rm MP} = 7.7$) has parameters $r_{\rm a,MR} = 0.2 \pm 0.1$ kpc, $r_{\rm a,MP} = 1.4$ kpc (with a lower limit of 0.5 kpc) and M/L$= 4.8^{+1.7}_{-1.3}$ $(\mathrm{M/L})_\odot$ (Fig. 5.18). This model matches the data well except in the first bin of the MR velocity dispersion profile, as the model predicts a dispersion which is too large, especially if we take into account the more precise value of 6.4 km s^{-1} indicated by the HR data for the second bin.

The quality of the fit for this MOND model is poorer than with for the best-fitting isothermal and NFW models.

The M/L ratio for the luminous component that we derived from the combined MR and MP fit remains very similar to the single component case. These best-fitting M/L in the V band are towards the higher end of what predicted for an ancient simple stellar population for a Salpeter IMF (Maraston 1998).

5.7 Discussion

Our analysis shows that taking into account the presence of the MR and MP components in Scl has important implications for the kinematic modeling of this galaxy. First of all, ignoring the presence of multiple components impacts the interpretation of modeling results. Secondly, as distinct tracers of the potential the MR and MP components when properly distinguished allow us to better constrain the mass distribution and content of Scl in comparison to the traditional single component approach.

5.7.1 The multi-component nature of Scl

The MR stars in Scl, which dominate the central regions, exhibit a strongly declining velocity dispersion profile. In contrast, the more spatially extended MP stars have a dispersion profile which is mildly declining with distance from the centre. This combination conspires to produce a nearly flat velocity dispersion profile when no distinction in metallicity is made and all the stars are considered together. This is because the colder velocity dispersion of the MR stars tends to lower the overall dispersion in the central regions, whereas the middle and outer regions are dominated by the hotter kinematics of the MP stars.

This interplay between MR and MP stars can explain the apparent contradictions found when comparing the results of previous kinematic studies of Scl, particularly if one takes into account the differences in the location and sample sizes. For example previous studies, none of which had metallicity information available, found systematically lower dispersions in the central regions because of the bias induced by preferentially sampling the MR population. Queloz et al. (1995) found a very low dispersion for Scl (6.2 ± 1.1 km s^{-1}) when observing the very central regions (the inner 0.15 deg) with a sample of only 23 stars, which can be readily explained by the fact that, inadvertedly, they were mostly probing the colder kinematics of the MR stars. In contrast, Westfall

et al. (2006), with a larger sample covering more of the galaxy, found a global dispersion $\sim$8 km s^{-1} out to 0.5 deg, and $\sim$11 km s^{-1} at larger radii, which is consistent with our findings (their Fig. 12).

It is possible that the combination of multiple components producing nearly flat global dispersion profiles is more common and may lead to the incorrent interpretation of kinematic modeling. Flat dispersion profiles, as seen in Scl, are better modelled by a constant, mildly tangential velocity anisotropy, as found by Kleyna et al. (2002), Łokas (2002) and Kazantzidis et al. (2004) to fit the global dispersion profiles of Draco and Fornax. As noted by Kazantzidis et al. (2004), this is in agreement with predictions from formation scenarios of dSphs, such as tidal stirring (Mayer et al. 2001a,b). However, tangential anisotropy is not required when considering the kinematics of the multiple components separately. In fact, in our analysis of the Scl dSph, radial or close to isotropic velocity ellipsoids are favoured by the indipendent kinematic modeling of the MR and MP stars. McConnachie et al. (2006) also showed that the shape of the overall velocity dispersion profile of Draco and Fornax can be reproduced by isotropic toy models assuming two components. It is thus important to accurately define the detailed properties of even these most simple small systems.

5.7.2 Comparison to ΛCDM models

The multi-component nature of Scl has allowed us to constrain fundamental properties such as its mass content and distribution. Our interpretation favours a cored profile; however a cusped profile such as the NFW model is also statistically consistent with these data. We can also use the derived properties of Scl to test further predictions of DM theories, such as the mass spectrum of satellite galaxies predicted to orbit the MW, and to put constraints on the nature of dark-matter.

In the Introduction (Sect. 5.1) we touched upon the "missing satellites problem" that challenges CDM theories. Most solutions to this problem propose a threshold in the peak circular velocity, $v_{\rm max}$, for the DM subhaloes in which dSphs are embedded. This prediction can be tested by measuring $v_{\rm max}$ for dSphs. However this is not a simple measurement.

From our analysis of Scl we have seen that the determination of $v_{\rm max}$ in the standard single component modeling is subject to several degeneracies. In particular, for an NFW profile the virial mass/concentration degeneracy does not allow us to constrain the $v_{\rm max}$ of the DM halo. This degeneracy is expecially severe in systems where the peak of the velocity curve occurs beyond the farthest point probed by the data (see also Strigari et al. 2006), as in Scl. However, with our two component modeling of Scl we were able to relieve this degeneracy and significantly constrain the range of $v_{\rm max}$ allowed by the data. For the best-fitting NFW models we find $v_{\rm max} = 24$ km s^{-1} when using only the LR data ($c = 20$, $M_v = 2.2^{+1.0}_{-0.7} \times 10^9\ M_\odot$) and $v_{\rm max} = 27.6$ km s^{-1} when adding the HR data ($c = 15$ and $M_v = 4.2^{+2.5}_{-1.7} \times 10^9\ M_\odot$). These values are a bit lower but not incompatible with what is predicted if dSphs are assumed to have formed their stars before reionization, but more difficult to reconcile with the values of $v_{\rm max} > 35$ km s^{-1} predicted by Stoehr et al. (2002) and Hayashi et al. (2003) if dSphs inhabit the most massive subhaloes.

At this point we could simply conclude that the peak circular velocity of Scl is

a bit lower than what is typically expected for CDM subhaloes. However, a proper comparison between predictions and observations should take into account how the properties of a subhalo (satellite), like its concentration, density profile etc, can be modified by interactions with the host galaxy. It is possible that the $v_{\rm max}$ values measured today for dSphs are not representative of what they were in the past, but that they have been lowered as a consequence of the fact that subhaloes lose mass because of the tidal forces exterted by their host halo. The change in $v_{\rm max}$ is related to the orbital history of the satellite and thus how strong has been the interaction with the host galaxy. Satellites that suffer dramatic mass loss will have their $v_{\rm max}$ reduced by as much as 50% (Hayashi et al. 2003; Kravtsov et al. 2004). For systems with pericentric distances $\gtrsim$50 kpc, mass loss because of tidal interaction is likely to be minimal and $v_{\rm max}$ changes only slightly (Fig. 3 in Kravtsov et al. 2004). Recent proper motion measurements for Scl suggest a pericentric distance of 70 kpc (Piatek et al. 2006) which would imply that the currently measured $v_{\rm max}$ resembles the initial value. However these proper motions still have large uncertainties and thus it is not possible to firmly establish the orbital history of Scl.

A possible way to circumvent the uncertainties in the comparison between predictions and observations is to use quantities which are both well determined observationally and are not expected to be significantly altered during the evolution of the satellite. One example is the DM mass within the extent of the light distribution. In this respect it is worth considering the suggestion of revisiting the missing satellites problem made by Strigari et al. (2007b). These authors proposed to use the mass enclosed within 0.6 kpc, $M_{0.6}$. They derived $M_{0.6}$ for the MW satellites using the latest kinematic information from the literature and compared the data to the predictions from the Via Lactea simulation (Diemand et al. 2007). They found that the observed $M_{0.6}$ cumulative function could be reproduced by assuming that either the dSphs were embedded in the earliest accreted subhaloes or that they were in the most massive haloes at the time of accretion (note that they did not use the observed satellite spatial distribution as a constraint). For the Scl dSph they found $M_{0.6} = 2.7 \pm 0.4 \times 10^7\ M_\odot$ assuming a CDM halo. For comparison, we find $M_{0.6} = 4.4^{+1.1}_{-0.8} \times 10^7\ M_\odot$ (where the errors are derived by marginalizing with respect to the other parameters) from our best-fitting NFW profile ($c = 20$). This value is larger than what found by Strigari et al. (2007b) but in 2σ agreement with their result.

The approach of using the mass enclosed within a certain point, be it within 0.6 kpc or the extent of the light distribution, seems to be promising and less subject to uncertainties. Obviously this requires homogeneity in the measurements of the different galaxies, whose mass should be considered out to the same radius.

An independent test on the nature of DM can be given by experiments devoted to detect γ-ray flux from DM haloes. In this context, γ-rays are produced by annihilation between weakly interacting particles, such as for instance WIMPS, which are good candidates for CDM. Strigari et al. (2007a) showed that, assuming that dSphs are embedded in smooth NFW haloes, the expected γ-ray flux depends on the NFW parameters such as the characteristic density ρ_s and the scale radius r_s, and from their analysis they found that Ursa Minor and Draco are the most promising targets in terms of expected γ-ray flux. Using the parameters from our best-fitting NFW model we find $\rho_s = 1.7 \times 10^7\ M_\odot\,{\rm kpc}^{-3}$ and $r_s = 1.7$ kpc, which give an expected flux $\sim 10^{-11}$

photons cm^{-2} s^{-1} from a region of 2 degrees radius centered on Scl assuming a smooth DM halo, slightly above the predictions of Strigari et al. (2007a) (their Fig. 3). This makes Scl a potentially interesting target for GLAST (see Strigari et al. 2007a, and references therein), although still fainter than Ursa Minor and Draco.

5.8 Summary and conclusions

We derived the l.o.s. velocity dispersion profile of the Sculptor dSph out to its nominal tidal radius using accurate velocities from low resolution (R ∼6500) VLT/FLAMES spectroscopic measurements of ∼ 470 RGB stars in the CaT region, supplemented by HR (R∼20000) velocities in the centre.

The observed global velocity dispersion profile is approximately constant around 9 km s^{-1} out to its last measured point at 1.3 deg (1.8 kpc). When taking into account the metallicity information, we find that MR stars exhibit a strongly declining velocity dispersion profile while the MP velocity dispersion profile is consistent with being nearly flat or mildly declining.

We compared the observed l.o.s. velocity dispersion profile to the predictions of DM models, in order to derive the Scl mass content, using a maximum likelihood method which takes into account the presence and percentage of MW foreground interlopers, and how this varies with radius.

Following the traditional approach, we first modeled Scl as a one component galaxy. In this case, we find that the results are subject to several degeneracies that do not allow us to distinguish between a cored and a cusped DM distribution.

Because of the two distinct kinematic components identified in Scl (Chapter 4) we were also able to model Scl as a two component system, using the MR and MP populations as distinct tracers of the same potential. This allowed us to break some of the degeneracies that plague single component modeling. Under the explored assumptions for the behaviour of the velocity anisotropy, some of the models are not able to simultaneously satisfy both the MR and MP velocity dispersion trends, and in particular they are unable to reproduce the central values of the MR velocity dispersion. From the combined fit of MR and MP stars we find that the best model is a cored profile with r_c =0.5 kpc and $M(< r_{\rm last}) = 3.4 \pm 0.7 \times 10^8\ M_\odot$, which gives an excellent representation of the data assuming an increasingly radial anisotropy. An NFW profile with $c = 20$ and a virial mass $M_v = 2.2^{+1.0}_{-0.7} \times 10^9\ M_\odot$ is also statistically consistent with the data, but it overpredicts the central velocity dispersion of the MR component. The mass enclosed within the last point by the NFW model is $M(< r_{\rm last}) = 2.2^{+1.0}_{-0.7} \times 10^8$ $M_\odot$, which is consistent with the cored profile value within 1σ. These values for the Scl mass within the last measured point do not confirm (by an order of magnitude) the suggestion that dSph galaxies might have a common mass scale of $4 \times 10^7\ M_\odot$ (Wilkinson et al. 2006). The scale radius $r_s = 1.7$ kpc derived from our best-fitting NFW model appear to confirm the suggestion made by Penarrubia et al. (2007) that the stellar component of dSphs is likely to be deeply embedded in their DM halo, resulting in a core radius-scale radius ratio of 0.07.

An alternative approach such as MOND is also statistically consistent with these data but less satisfactory than any of the best fitting dark matter haloes fit under the

velocity anisotropy assumptions we used. A velocity ellipsoid which is tangential in the central region and becomes radial in the outskirts would, however, likely improve the quality of fit both for an NFW model and a MOND approach.

We conclude that the mass of Scl is one order of magnitude larger than was derived in previous measurements (Queloz et al. 1995) and that the favoured mass distribution is a cored profile with $r_c = 0.5$ kpc assuming an Osipkov-Merritt velocity anisotropy.

The results from such a large and spatially extended dataset which combines kinematic and metallicity information clearly shows that attention should be paid to the way targets are selected even in these seemingly simple systems.

The use of the kinematics of distinct stellar populations to help breaking the mass distribution/velocity anisotropy degeneracy has proved very useful. Since most of the dSphs satellites of the Milky Way show multiple stellar components, the technique pioneered here should be applied more widely in the future.

References

Aaronson, M. 1983, ApJ, 266, L11

Begeman, K. G., Broeils, A. H., & Sanders, R. H. 1991, MNRAS, 249, 523

Bellazzini, M., Ferraro, F. R., Origlia, L., Pancino, E., Monaco, L., & Oliva, E. 2002, AJ, 124, 3222

Belokurov, V., Zucker, D. B., Evans, N. W., Kleyna, J. T., Koposov, S., Hodgkin, S. T., Irwin, M. J., Gilmore, G., Wilkinson, M. I., Fellhauer, M., Bramich, D. M., Hewett, P. C., Vidrih, S., De Jong, J. T. A., Smith, J. A., Rix, H.-W., Bell, E. F., Wyse, R. F. G., Newberg, H. J., Mayeur, P. A., Yanny, B., Rockosi, C. M., Gnedin, O. Y., Schneider, D. P., Beers, T. C., Barentine, J. C., Brewington, H., Brinkmann, J., Harvanek, M., Kleinman, S. J., Krzesinski, J., Long, D., Nitta, A., & Snedden, S. A. 2007, ApJ, 654, 897

Belokurov, V., Zucker, D. B., Evans, N. W., Wilkinson, M. I., Irwin, M. J., Hodgkin, S., Bramich, D. M., Irwin, J. M., Gilmore, G., Willman, B., Vidrih, S., Newberg, H. J., Wyse, R. F. G., Fellhauer, M., Hewett, P. C., Cole, N., Bell, E. F., Beers, T. C., Rockosi, C. M., Yanny, B., Grebel, E. K., Schneider, D. P., Lupton, R., Barentine, J. C., Brewington, H., Brinkmann, J., Harvanek, M., Kleinman, S. J., Krzesinski, J., Long, D., Nitta, A., Smith, J. A., & Snedden, S. A. 2006, ApJ, 647, L111

Benson, A. J., Frenk, C. S., Lacey, C. G., Baugh, C. M., & Cole, S. 2002, MNRAS, 333, 177

Binney, J. & Mamon, G. A. 1982, MNRAS, 200, 361

Binney, J. & Merrifield, M. 1998, Galactic astronomy (Galactic astronomy / James Binney and Michael Merrifield. Princeton, NJ : Princeton University Press, 1998. (Princeton series in astrophysics) QB857 .B522 1998)

Binney, J. & Tremaine, S. 1987, Galactic dynamics (Princeton, NJ, Princeton University Press, 1987, 747 p.)

Bullock, J. S., Kolatt, T. S., Sigad, Y., Somerville, R. S., Kravtsov, A. V., Klypin, A. A., Primack, J. R., & Dekel, A. 2001, MNRAS, 321, 559

Bullock, J. S., Kravtsov, A. V., & Weinberg, D. H. 2000, ApJ, 539, 517

Cembranos, J. A., Feng, J. L., Rajaraman, A., & Takayama, F. 2005, Physical Review Letters, 95, 181301

Dalcanton, J. J. & Hogan, C. J. 2001, ApJ, 561, 35

de Blok, W. J. G., McGaugh, S. S., & Rubin, V. C. 2001, AJ, 122, 2396

Diemand, J., Kuhlen, M., & Madau, P. 2007, ApJ, 657, 262

Diemand, J., Zemp, M., Moore, B., Stadel, J., & Carollo, C. M. 2005, MNRAS, 364, 665

Douglas, N. G., Napolitano, N. R., Romanowsky, A. J., Coccato, L., Kuijken, K., Merrifield, M. R., Arnaboldi, M., Gerhard, O., Freeman, K. C., Merrett, H. R., Noordermeer, E., & Capaccioli, M. 2007, ArXiv Astrophysics e-prints

Dubinski, J. & Carlberg, R. G. 1991, ApJ, 378, 496

Emsellem, E., Cappellari, M., Peletier, R. F., McDermid, R. M., Bacon, R., Bureau, M., Copin, Y., Davies, R. L., Krajnović, D., Kuntschner, H., Miller, B. W., & de Zeeuw, P. T. 2004, MNRAS, 352, 721

Famaey, B. & Binney, J. 2005, MNRAS, 363, 603

Flores, R. A. & Primack, J. R. 1994, ApJ, 427, L1

Gentile, G., Salucci, P., Klein, U., & Granato, G. L. 2007, MNRAS, 375, 199

Gerhard, O. E. & Spergel, D. N. 1992, ApJ, 389, L9

Hargreaves, J. C., Gilmore, G., & Annan, J. D. 1996, MNRAS, 279, 108

Hargreaves, J. C., Gilmore, G., Irwin, M. J., & Carter, D. 1994, MNRAS, 271, 693

Hayashi, E. & Navarro, J. F. 2006, MNRAS, 373, 1117

Hayashi, E., Navarro, J. F., Taylor, J. E., Stadel, J., & Quinn, T. 2003, ApJ, 584, 541

Illingworth, G. 1976, ApJ, 204, 73

Kaplinghat, M. 2005, Phys. Rev. D, 72, 063510

Kazantzidis, S., Mayer, L., Mastropietro, C., Diemand, J., Stadel, J., & Moore, B. 2004, ApJ, 608, 663

Kent, S. M. 1987, AJ, 93, 816

Klessen, R. S. & Kroupa, P. 1998, ApJ, 498, 143

Kleyna, J., Wilkinson, M. I., Evans, N. W., Gilmore, G., & Frayn, C. 2002, MNRAS, 330, 792

Kleyna, J. T., Wilkinson, M. I., Evans, N. W., & Gilmore, G. 2001, ApJ, 563, L115

Kleyna, J. T., Wilkinson, M. I., Gilmore, G., & Evans, N. W. 2003, ApJ, 588, L21

Klypin, A., Kravtsov, A. V., Valenzuela, O., & Prada, F. 1999, ApJ, 522, 82

Koch, A., Kleyna, J. T., Wilkinson, M. I., Grebel, E. K., Gilmore, G. F., Evans, N. W., Wyse, R. F. G., & Harbeck, D. R. 2007, AJ, 134, 566

Kravtsov, A. V., Gnedin, O. Y., & Klypin, A. A. 2004, ApJ, 609, 482

Kroupa, P. 1997, New Astronomy, 2, 139

Lanzoni, B. & Ciotti, L. 2003, A&A, 404, 819

Lin, D. N. C. & Faber, S. M. 1983, ApJ, 266, L21

Łokas, E. L. 2002, MNRAS, 333, 697

Łokas, E. L. & Mamon, G. A. 2003, MNRAS, 343, 401

Majewski, S. R., Ostheimer, J. C., Kunkel, W. E., & Patterson, R. J. 2000, AJ, 120, 2550

Mamon, G. A. & Łokas, E. L. 2005, MNRAS, 363, 705

Maraston, C. 1998, MNRAS, 300, 872

Mateo, M., Olszewski, E., Welch, D. L., Fischer, P., & Kunkel, W. 1991, AJ, 102, 914

Mateo, M. L. 1998, ARA&A, 36, 435

Mayer, L., Governato, F., Colpi, M., Moore, B., Quinn, T., Wadsley, J., Stadel, J., & Lake, G. 2001a, ApJ, 559, 754

—. 2001b, ApJ, 547, L123

McConnachie, A. W., Penarrubia, J., & Navarro, J. F. 2006, ArXiv Astrophysics e-prints

McGaugh, S. S. & de Blok, W. J. G. 1998, ApJ, 499, 41

Merritt, D. 1985, MNRAS, 214, 25P

Milgrom, M. 1983, ApJ, 270, 365

—. 1988, ApJ, 333, 689

Moore, B. 1994, Nature, 370, 629

Moore, B., Ghigna, S., Governato, F., Lake, G., Quinn, T., Stadel, J., & Tozzi, P. 1999, ApJ, 524, L19

Morrison, H. L., Olszewski, E. W., Mateo, M., Norris, J. E., Harding, P., Dohm-Palmer, R. C., & Freeman, K. C. 2001, AJ, 121, 283

Muñoz, R. R., Majewski, S. R., Zaggia, S., Kunkel, W. E., Frinchaboy, P. M., Nidever, D. L., Crnojevic, D., Patterson, R. J., Crane, J. D., Johnston, K. V., Sohn, S. T., Bernstein, R., & Shectman, S. 2006, ApJ, 649, 201

Navarro, J. F., Frenk, C. S., & White, S. D. M. 1996, ApJ, 462, 563

—. 1997, ApJ, 490, 493

Osipkov, L. P. 1979, Soviet Astronomy Letters, 5, 42

Palma, C., Majewski, S. R., Siegel, M. H., Patterson, R. J., Ostheimer, J. C., & Link, R. 2003, AJ, 125, 1352

Penarrubia, J., McConnachie, A., & Navarro, J. F. 2007, ArXiv Astrophysics e-prints

Piatek, S., Pryor, C., Bristow, P., Olszewski, E. W., Harris, H. C., Mateo, M., Minniti, D., & Tinney, C. G. 2006, AJ, 131, 1445

Pryor, C., McClure, R. D., Fletcher, J. M., & Hesser, J. E. 1988, in IAU Symposium, Vol. 126, The Harlow-Shapley Symposium on Globular Cluster Systems in Galaxies, ed. J. E. Grindlay & A. G. D. Philip, 661

Queloz, D., Dubath, P., & Pasquini, L. 1995, A&A, 300, 31

Robin, A. C., Reylé, C., Derrière, S., & Picaud, S. 2003, A&A, 409, 523

Ségall, M., Ibata, R. A., Irwin, M. J., Martin, N. F., & Chapman, S. 2007, MNRAS, 375, 831

Stoehr, F., White, S. D. M., Tormen, G., & Springel, V. 2002, MNRAS, 335, L84

Strigari, L. E., Bullock, J. S., & Kaplinghat, M. 2007a, ApJ, 657, L1

Strigari, L. E., Bullock, J. S., Kaplinghat, M., Diemand, J., Kuhlen, M., & Madau, P. 2007b, ArXiv e-prints, 704

Strigari, L. E., Bullock, J. S., Kaplinghat, M., Kravtsov, A. V., Gnedin, O. Y., Abazajian, K., & Klypin, A. A. 2006, ApJ, 652, 306

Strigari, L. E., Kaplinghat, M., & Bullock, J. S. 2007c, Phys. Rev. D, 75, 061303

Suntzeff, N. B., Mateo, M., Terndrup, D. M., Olszewski, E. W., Geisler, D., & Weller, W. 1993, ApJ, 418, 208

Swaters, R. A., Madore, B. F., & Trewhella, M. 2000, ApJ, 531, L107

Walker, M. G., Mateo, M., Olszewski, E. W., Bernstein, R., Wang, X., & Woodroofe, M. 2006, AJ, 131, 2114

Walsh, S. M., Jerjen, H., & Willman, B. 2007, ArXiv e-prints, 705

Wechsler, R. H., Bullock, J. S., Primack, J. R., Kravtsov, A. V., & Dekel, A. 2002, ApJ, 568, 52

Westfall, K. B., Majewski, S. R., Ostheimer, J. C., Frinchaboy, P. M., Kunkel, W. E., Patterson, R. J., & Link, R. 2006, AJ, 131, 375

Wilkinson, M. I., Kleyna, J. T., Wyn Evans, N., Gilmore, G. F., Read, J. I., Koch, A., Grebel, E. K., & Irwin, M. J. 2006, in EAS Publications Series, Vol. 20, EAS Publications Series, ed. G. A. Mamon, F. Combes, C. Deffayet, & B. Fort, 105–112

Willman, B., Blanton, M. R., West, A. A., Dalcanton, J. J., Hogg, D. W., Schneider, D. P., Wherry, N., Yanny, B., & Brinkmann, J. 2005a, AJ, 129, 2692

Willman, B., Dalcanton, J. J., Martinez-Delgado, D., West, A. A., Blanton, M. R., Hogg, D. W., Barentine, J. C., Brewington, H. J., Harvanek, M., Kleinman, S. J., Krzesinski, J., Long, D., Neilsen, Jr., E. H., Nitta, A., & Snedden, S. A. 2005b, ApJ, 626, L85

Wojtak, R., Łokas, E. L., Mamon, G. A., Gottlöber, S., Prada, F., & Moles, M. 2007, A&A, 466, 437

Zucker, D. B., Belokurov, V., Evans, N. W., Kleyna, J. T., Irwin, M. J., Wilkinson, M. I., Fellhauer, M., Bramich, D. M., Gilmore, G., Newberg, H. J., Yanny, B., Smith, J. A., Hewett, P. C., Bell, E. F., Rix, H.-W., Gnedin, O. Y., Vidrih, S., Wyse, R. F. G., Willman, B., Grebel, E. K., Schneider, D. P., Beers, T. C., Kniazev, A. Y., Barentine, J. C., Brewington, H., Brinkmann, J., Harvanek, M., Kleinman, S. J., Krzesinski, J., Long, D., Nitta, A., & Snedden, S. A. 2006a, ApJ, 650, L41

Zucker, D. B., Belokurov, V., Evans, N. W., Wilkinson, M. I., Irwin, M. J., Sivarani, T., Hodgkin, S., Bramich, D. M., Irwin, J. M., Gilmore, G., Willman, B., Vidrih, S., Fellhauer, M., Hewett, P. C., Beers, T. C., Bell, E. F., Grebel, E. K., Schneider, D. P., Newberg, H. J., Wyse, R. F. G., Rockosi, C. M., Yanny, B., Lupton, R., Smith, J. A., Barentine, J. C., Brewington, H., Brinkmann, J., Harvanek, M., Kleinman, S. J., Krzesinski, J., Long, D., Nitta, A., & Snedden, S. A. 2006b, ApJ, 643, L103

Appendix 5.A Contour plots from Scl two components modeling

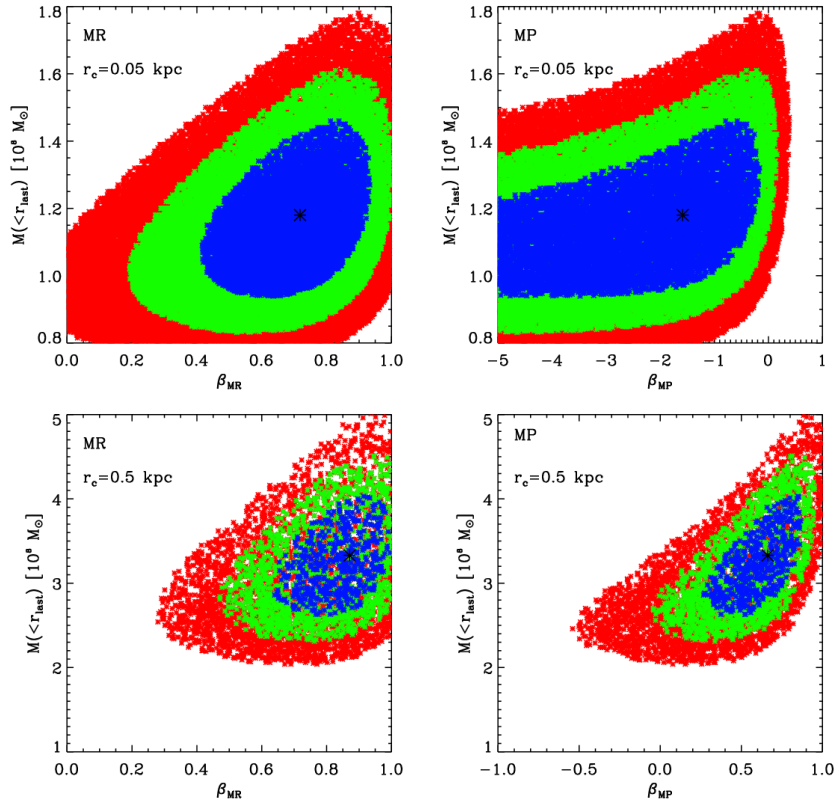

Figure 5.A1: Contour plot of $\Delta\chi^2$ corresponding to a probability of the 68.3%, 95.4% and 99.73% (1-2-3σ regions) for the isothermal models in the hypothesis of β constant with the radius shown in Fig. 5.12 (top: $r_c = 0.05$ kpc; bottom: $r_c = 0.5$ kpc; left: MR; right: MP). Hereafter for the joint fit of MR and MP stars we are treating the χ^2 distribution as a 3 parameters distribution, and we plot the projections of the 3D probability region onto the considered parameter plane.

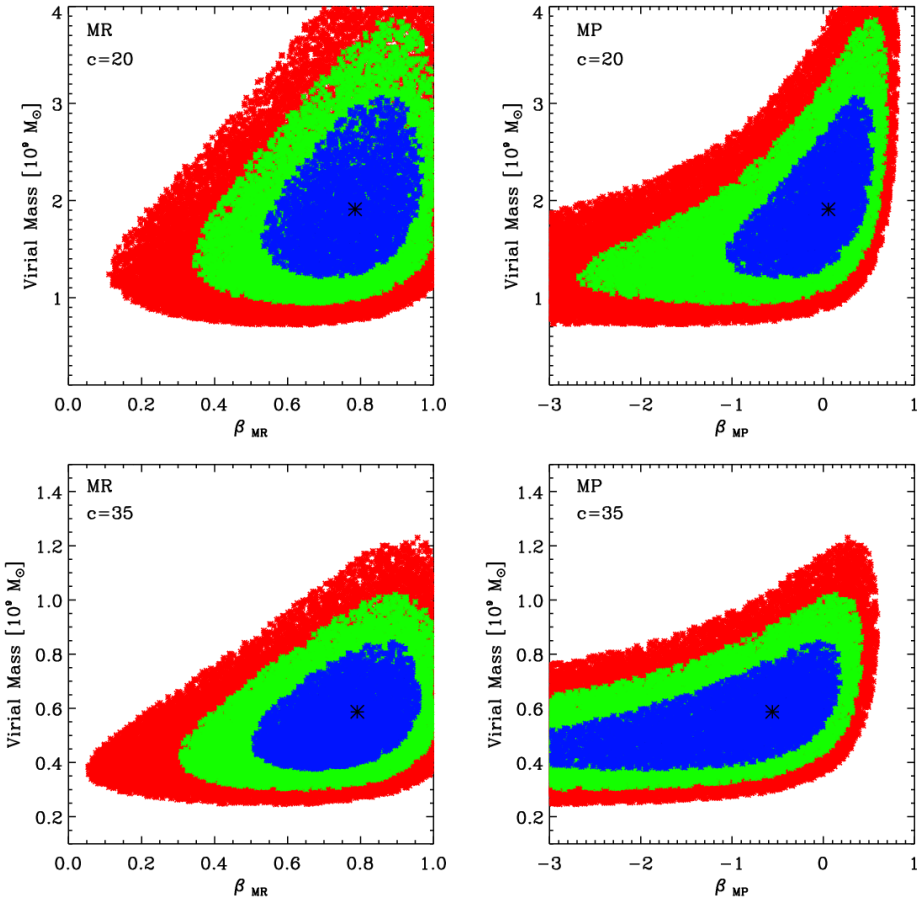

Figure 5.A2: Contour plot of $\Delta\chi^2$ corresponding to a probability of the 68.3%, 95.4% and 99.73% (1-2-3σ regions) for the NFW models in the hypothesis of β constant with the radius shown in Fig. 5.13 (top: $c = 20$; bottom: $c = 35$; left: MR; right: MP).

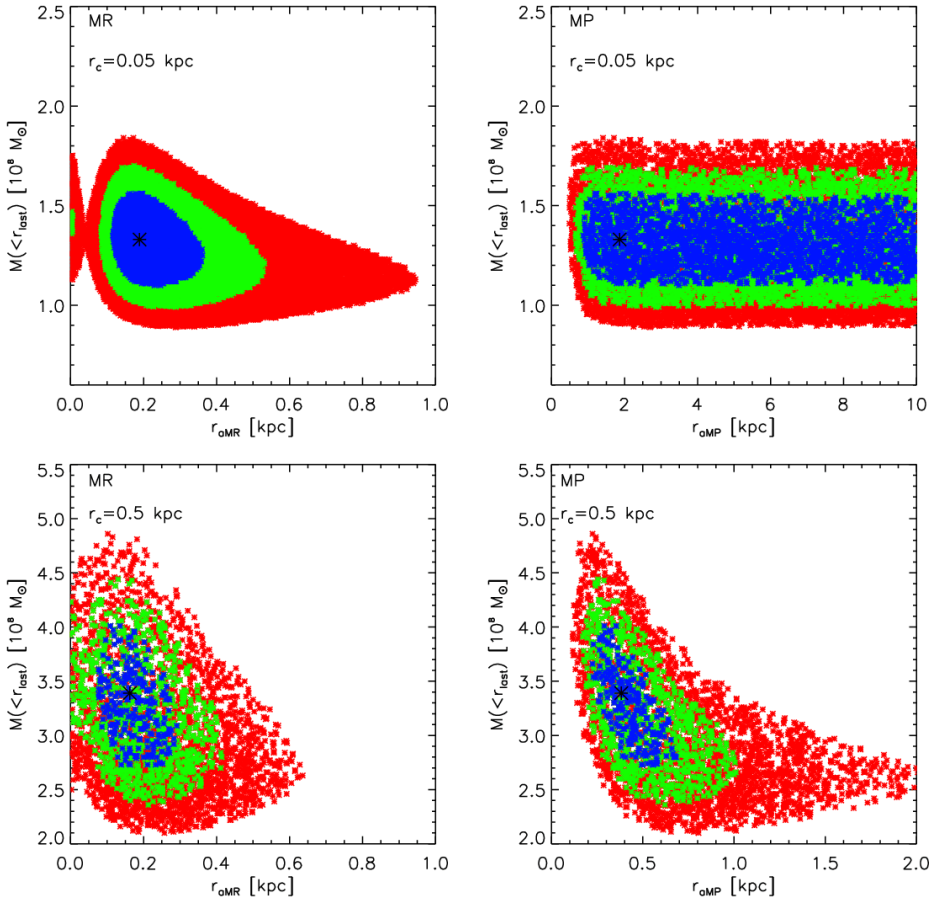

Figure 5.A3: Contour plot of $\Delta\chi^2$ corresponding to a probability of the 68.3%, 95.4% and 99.73% (1-2-3σ regions) for the isothermal models in the hypothesis of $\beta_{\rm OM}$ shown in Fig. 5.14 (top: $r_c = 0.05$ kpc; bottom: $r_c = 0.5$ kpc; left: MR; right: MP).

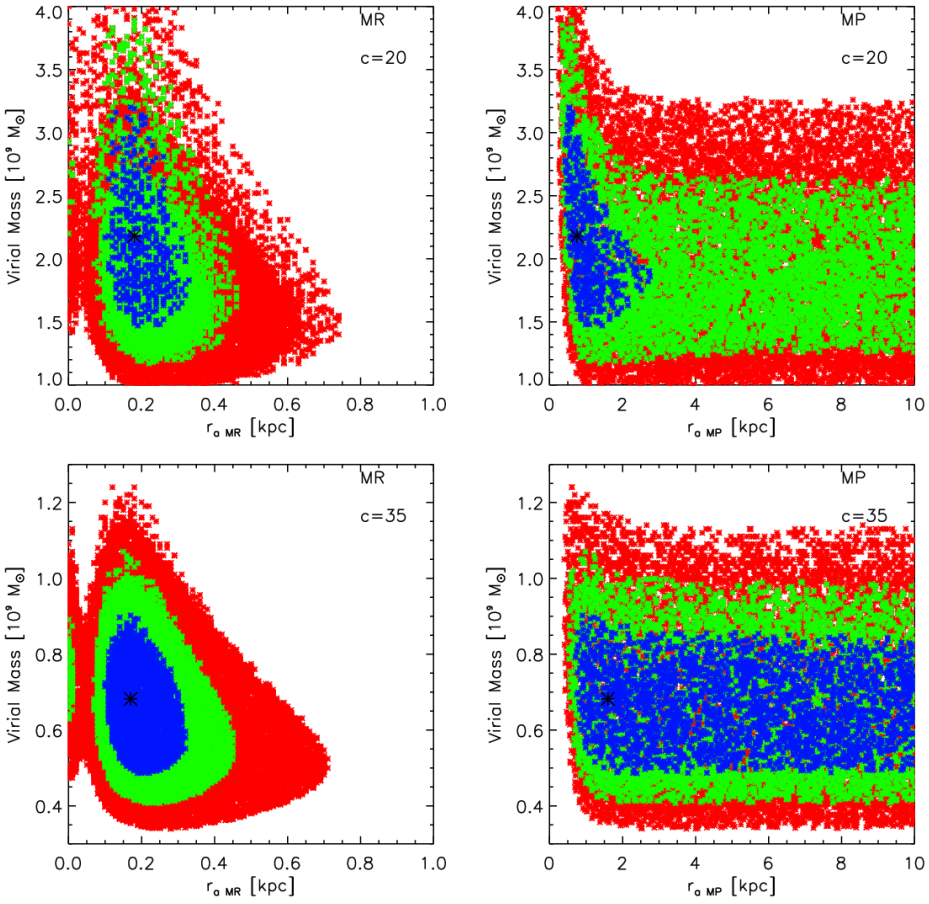

Figure 5.A4: Contour plot of $\Delta\chi^2$ corresponding to a probability of the 68.3%, 95.4% and 99.73% (1-2-3σ regions) for the NFW models in the hypothesis of $\beta_{\rm OM}$ shown in Fig. 5.15 (top: $c = 20$; bottom: $c = 35$; left: MR; right: MP).

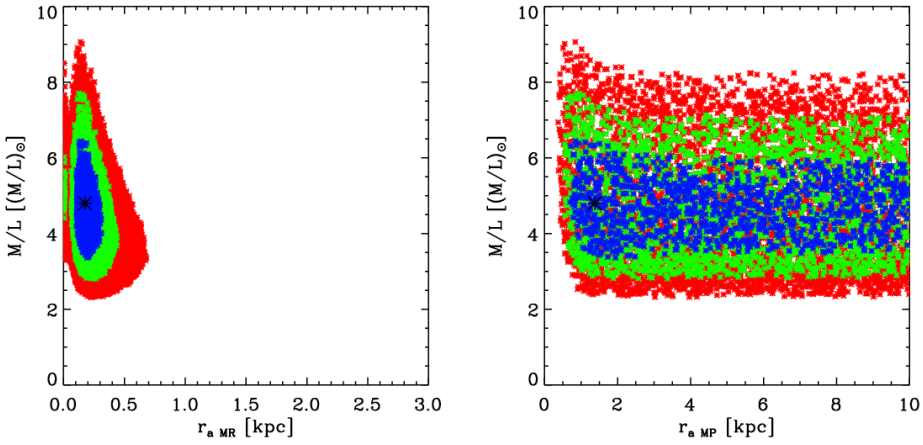

Figure 5.A5: Contour plots of $\Delta\chi^2$ corresponding to a probability of the 68.3%, 95.4% and 99.73% (1-2-3σ regions) relative to the best-fitting MOND model shown in Fig. 5.18 for MR (left) and MP (right) stars.